Nano Research

ISSN 1998-0124 CN 11-5974/O4
https://doi.org/10.26599/NR.2026.94909304

Research Article

Salt-regulated interfacial desolvation suppresses Co-intercalation of strongly coordinating ether-based electrolytes for fast-charging lithium-ion batteries

Tian Gao[1], Xiaowang Tu[1], Zicheng Zhao[1], Qiang Yu[2](✉), Zhenming Xu[1], Mingbo Zheng[1], Jianyu Shi[1], Yujie Zhou[1], Junfeng Chen[3](✉), Yi Pei[4], Zhenhui Liu[1](✉)

[1] College of Material Science and Engineering, Jiangsu Key Laboratory of Materials and Technology for Energy Conversion, Nanjing University of Aeronautics and Astronautics, Nanjing 210016, China

[2] Laoshan Laboratory, Qingdao 266237, China

[3] School of Materials Science and Engineering, Fuzhou University, Fuzhou 350108, China, State Key Laboratory of Green and Efficient Development of Phosphorus Resources, Fuzhou University, Fuzhou 350108, China

[4] Shenzhen Research Institute, Nanjing University of Aeronautics and Astronautics, Shenzhen 518110, China

Nano Res., **Just Accepted Manuscript** • https://doi.org/10.26599/NR.2026.94909304

https://www.sciopen.com/journal/1998-0124 on Nov. 1, 2026

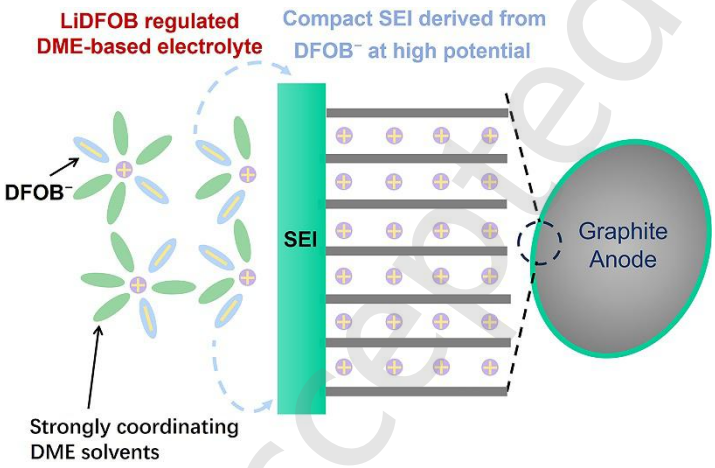
© The Authors(s)

Just Accepted

This is a "Just Accepted" manuscript, which has been examined by the peer-review process and has been accepted for publication. A "Just Accepted" manuscript is published online shortly after its acceptance,which is prior to technical editing and formatting and author proofing. Tsinghua University Press (TUP) provides "Just Accepted" as an optional and free service which allows authors to make their results available to the research community as soon as possible after acceptance. After a manuscript has been technically edited and formatted, and the page proofs have been corrected, it will be removed from the "Just Accepted" web site and published officially with volume and article number (e.g., *Nano Research*, **2025**, *18*, 94906990). Please note that technical editing may introduce minor changes to the manuscript text and/or graphics which may affect the content, and all legal disclaimers that apply to the journal pertain. In no event shall TUP be held responsible for errors or consequences arising from the use of any information contained in these "Just Accepted" manuscripts. To cite this anuscript please use its Digital Object Identifier (DOI®),which is identical for all formats of publication.

Table of contents

Salt-regulated 1 M LiDFOB/DME electrolyte suppresses solvent co-intercalation in graphite, enabling fast charging, as $DFOB^-$ reduces DME within the Li^+ solvation sheath to form a B-containing, LiF-enriched stable SEI. This yields ~325 mAh g^{-1} at 5 C in half-cells and 80.2% capacity retention after 300 cycles at 4 C in full cells.



Just Accepted

Research Article

Salt-regulated interfacial desolvation suppresses Co-intercalation of strongly coordinating ether-based electrolytes for fast-charging lithium-ion batteries

Tian Gao [1], Xiaowang Tu [1], Zicheng Zhao [1], Qiang Yu [2] ✉, Zhenming Xu [1], Mingbo Zheng [1], Jianyu Shi [1], Yujie Zhou [1], Junfeng Chen [3] ✉, Yi Pei [4], Zhenhui Liu [1] ✉

[1] College of Material Science and Engineering, Jiangsu Key Laboratory of Materials and Technology for Energy Conversion, Nanjing University of Aeronautics and Astronautics, Nanjing 210016, China
[2] Laoshan Laboratory, Qingdao 266237, China
[3] School of Materials Science and Engineering, Fuzhou University, Fuzhou 350108, China, State Key Laboratory of Green and Efficient Development of Phosphorus Resources, Fuzhou University, Fuzhou 350108, China
[4] Shenzhen Research Institute, Nanjing University of Aeronautics and Astronautics, Shenzhen 518110, China

Received: 28 September 2026; **Revised: 27 October 2026**; **Accepted: 1 November 2026**

✉Address correspondence to Qiang Yu, qyu1@lsnl.cn; Zhenhui Liu, lzh0328@nuaa.edu.cn; Junfeng Chen, chenjunfeng@fzu.edu.cn

Cite this article: *Nano Research*, 2027, 20, 94909304 https://doi.org/10.26599/NR.2026.94909304

ABSTRACT: Ether-based electrolytes are highly attractive for fast-charging lithium-ion batteries due to their low viscosity and rapid Li^+ transport kinetics, yet their practical application with graphite anodes is severely hampered by solvent co-intercalation. Herein, we propose a salt-regulated ether electrolyte with a conventional concentration of 1 M, employing lithium difluoro(oxalato)borate (LiDFOB) as the sole lithium salt in a 1,2-dimethoxyethane/fluoroethylene carbonate (DME/FEC, 95/5, v/v) solvent mixture to simultaneously regulate the Li^+ solvation structure and interfacial chemistry. Theoretical calculations and experimental characterizations demonstrate that $DFOB^-$ competitively coordinates Li^+, thereby reducing the contribution of DME to the primary solvation sheath. Meanwhile, early interfacial reactions of LiDFOB facilitate the formation of a compact B-containing solid electrolyte interphase (SEI) on graphite, which progressively enriches in LiF during lithiation and thus suppresses solvent co-intercalation. Electrolyte-exchange experiments further verify that the preformed SEI retains its protective capability even in co-intercalation-prone electrolytes. The designed electrolyte exhibits a high ionic conductivity of 10.37 mS cm^{-1} and superior interfacial stability. Graphite half-cells deliver a reversible capacity of approximately 325 mAh g^{-1} at 5 C, while high-loading Gr||NCM811 full cells retain 80.2% of their stabilized capacity after 300 cycles at 4 C with a 4.4 V upper cutoff. This work offers new mechanistic insights into solvent co-intercalation and establishes a practical salt-regulation strategy for long-life fast-charging lithium-ion batteries.

KEYWORDS: lithium-ion battery, fast-charging electrolyte, graphite anode, ether-based solvents, co-intercalation, interface stability

1. Introduction

The rapidly growing demand for fast charging and high-power operation in electric vehicles and emerging energy-storage technologies has placed increasingly stringent requirements on the kinetic performance of lithium-ion batteries (LIBs) [1–5]. As the medium connecting the cathode and anode, the electrolyte governs both bulk Li^+ transport and interfacial ion-transfer processes and therefore plays a decisive role in determining battery rate capability [6,7]. Conventional carbonate electrolytes, particularly ethylene carbonate (EC)-based systems, have enabled the widespread commercialization of graphite anodes because EC can preferentially decompose on graphite to form a stable solid electrolyte interphase (SEI), thereby supporting reversible Li^+ intercalation and deintercalation [8–12]. However, the relatively strong Li^+–carbonate coordination and comparatively high viscosity of carbonate electrolytes increase the kinetic penalty associated with Li^+ transport and interfacial desolvation, resulting in substantial polarization under high-rate operation [13–15]. Therefore, developing electrolyte

Just Accepted

systems that simultaneously enable rapid Li^+ transport and stable graphite interfacial chemistry is essential for next-generation fast-charging LIBs [16,17].

Ether-based electrolytes are attractive alternatives because of their intrinsically low viscosity, favorable electrode wettability, and rapid Li^+ transport characteristics [1,18–21]. Among them, 1,2-dimethoxyethane (DME) is particularly appealing owing to its relatively low cost, established industrial supply chain, and excellent transport properties [22]. These characteristics have led to extensive use of DME-based electrolytes in lithium-metal batteries [23,24]. However, their application in technologically mature graphite-based LIBs remains challenging because DME exhibits severe compatibility issues with graphite [25,26]. During the initial lithiation process, solvated Li^+–DME complexes can enter the graphite galleries before an effective protective interphase is established, resulting in solvent co-intercalation, interlayer expansion, graphite exfoliation, and irreversible structural degradation [27]. Consequently, the intrinsic kinetic advantages of DME cannot be directly translated into high-rate graphite-based LIBs. Resolving this incompatibility would therefore provide an attractive route to combine the low cost and fast transport of DME with the technological maturity and high reversibility of graphite anodes [3].

The tendency of DME to co-intercalate into graphite originates from the coupling between bulk solvation chemistry and interfacial reaction chemistry [25,26,28]. In the bulk electrolyte, the strong participation of DME in Li^+ coordination stabilizes solvent-rich Li^+ complexes, making complete removal of coordinated DME molecules before graphite intercalation kinetically unfavorable [14,26,29]. At the electrode interface, DME does not readily generate a sufficiently protective interphase at potentials preceding substantial solvent co-intercalation [23,25]. As a consequence, solvated Li^+–DME species can penetrate into the graphite galleries before an effective SEI barrier is established [25,27]. Highly concentrated electrolytes (HCEs) and localized high-concentration electrolytes (LHCEs) have therefore been widely employed to mitigate ether co-intercalation [13,15,30]. Increasing the salt concentration enhances anion participation in the Li^+ solvation sheath, decreases the fraction of solvent-dominated complexes, and favors the formation of inorganic-rich interphases [13,15,22,31–35]. Nevertheless, the high salt contents required by these strategies substantially increase electrolyte cost and viscosity and can compromise ionic transport [7]. Film-forming additives can also alleviate solvent co-intercalation, but excessive additive contents may partly sacrifice the low-viscosity and fast-transport advantages of DME [6]. More importantly, these approaches generally rely on increasing salt or additive content rather than intrinsically exploiting salt chemistry to simultaneously regulate the bulk solvation structure and early interfacial reactions. A conventional-concentration ether electrolyte capable of addressing both aspects therefore remains highly desirable [1].

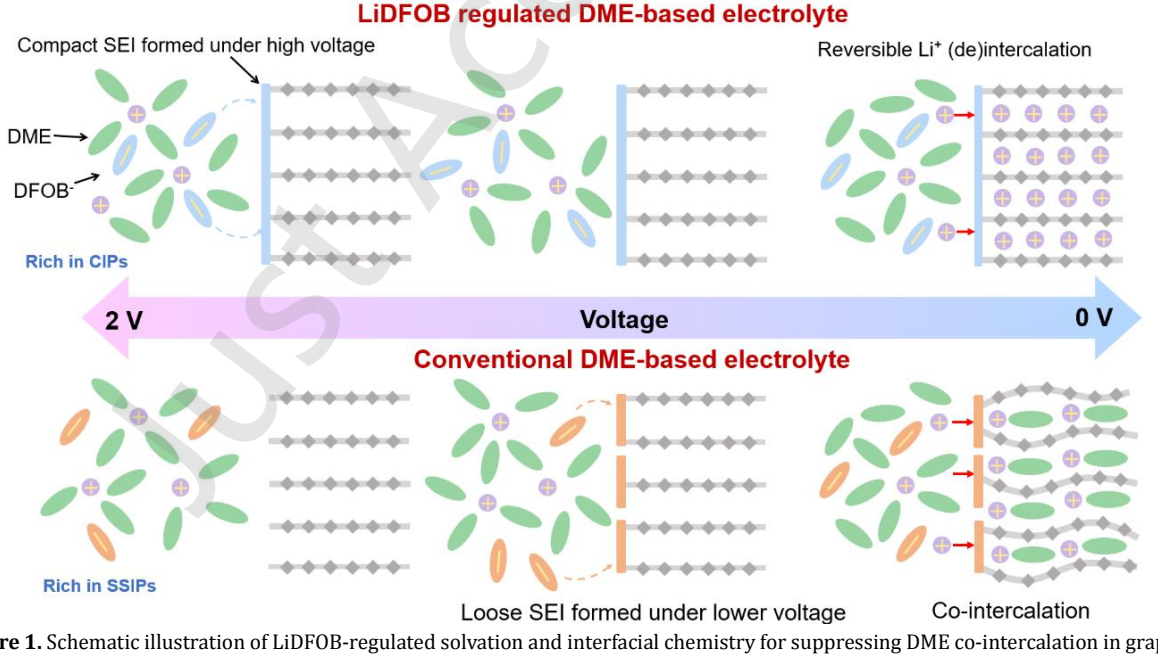


Figure 1. Schematic illustration of LiDFOB-regulated solvation and interfacial chemistry for suppressing DME co-intercalation in graphite

Here, we employ lithium difluoro(oxalato)borate (LiDFOB) as the sole lithium salt to formulate a conventional-concentration electrolyte of 1 M in DME/FEC (95/5, v/v). As schematically illustrated in Figure 1, this strategy suppresses DME co-intercalation through the coupled regulation of Li^+ solvation and graphite interfacial chemistry. $DFOB^-$ participates in Li^+ coordination, reducing the contribution of DME to the primary solvation sheath [22,23]. Meanwhile, early interfacial reactions involving LiDFOB, together with FEC-assisted passivation, promote the formation of a protective, boron-containing interphase on graphite [6,9,10]. The combination of solvation regulation and interfacial protection improves the compatibility of the DME-based electrolyte with graphite. Notably, electrolyte-replacement experiments demonstrate that once the LiDFOB-derived SEI is established, graphite remains resistant to co-intercalation even after exposure to otherwise incompatible electrolytes, highlighting the critical role of the preformed interphase.

Just Accepted

Benefiting from the synergistic regulation of solvation and interfacial chemistry, the electrolyte maintains a high ionic conductivity of 10.37 mS cm^{-1} while enabling graphite half-cells to deliver approximately 325 mAh g^{-1} at 5 C. High-loading Gr||NCM811 full cells further retain 80.2% of their stabilized capacity after 300 cycles at 4 C with an upper cutoff voltage of 4.4 V. This work establishes a salt-regulated strategy for stabilizing conventional-concentration DME electrolytes toward graphite and provides mechanistic insight into the coupled roles of solvation chemistry and interfacial passivation in suppressing solvent co-intercalation.

2. Results and Discussion

To understand the molecular origin of DME-induced solvent co-intercalation, the intrinsic solvation characteristics of EC and DME were first investigated through theoretical calculations. Electrostatic potential (ESP) distributions, analyzed using the Multiwfn program, reveal distinct electronic environments around the oxygen coordination sites of EC and DME (Figure 2a) [36–38]. The carbonyl oxygen of EC exhibits a highly localized electron-rich region, whereas the ether oxygen atoms of DME display a more distributed electron density. Although individual ether oxygen sites possess weaker electron-donating characteristics, the flexible bidentate structure of DME enables simultaneous coordination with Li^+ through two oxygen atoms, facilitating the formation of stable chelated Li^+–DME complexes.

Molecular binding energy calculations further reveal differences in the coordination behavior of EC and DME (Figure 2b). Compared with coordination by a single DME molecule, the Li^+ complex containing two DME molecules exhibits a more negative binding energy, indicating greater overall stabilization of the complex. At comparable oxygen coordination numbers, EC-containing complexes exhibit more negative binding energies. However, the coordination geometries differ: EC coordinates through its carbonyl oxygen, whereas DME can form bidentate chelates through its two ether oxygen atoms. These results highlight the need to consider both binding strength and coordination geometry when discussing solvent removal prior to Li^+ intercalation into graphite.

The size comparison further illustrates the potential structural consequences of solvent co-intercalation (Figure 2c). The calculated minimum van der Waals thicknesses of the Li^+–EC and Li^+–DME complexes are 4.18 and 4.77 Å, respectively, both exceeding the graphite interlayer spacing of 3.35 Å. Insertion of these complexes while retaining their coordinated solvent would therefore require expansion of the graphite galleries. The larger thickness of the Li^+–DME complex highlights the potential structural disturbance associated with its co-intercalation and underscores the importance of interfacial protection that permits Li^+ intercalation while restricting solvent entry.

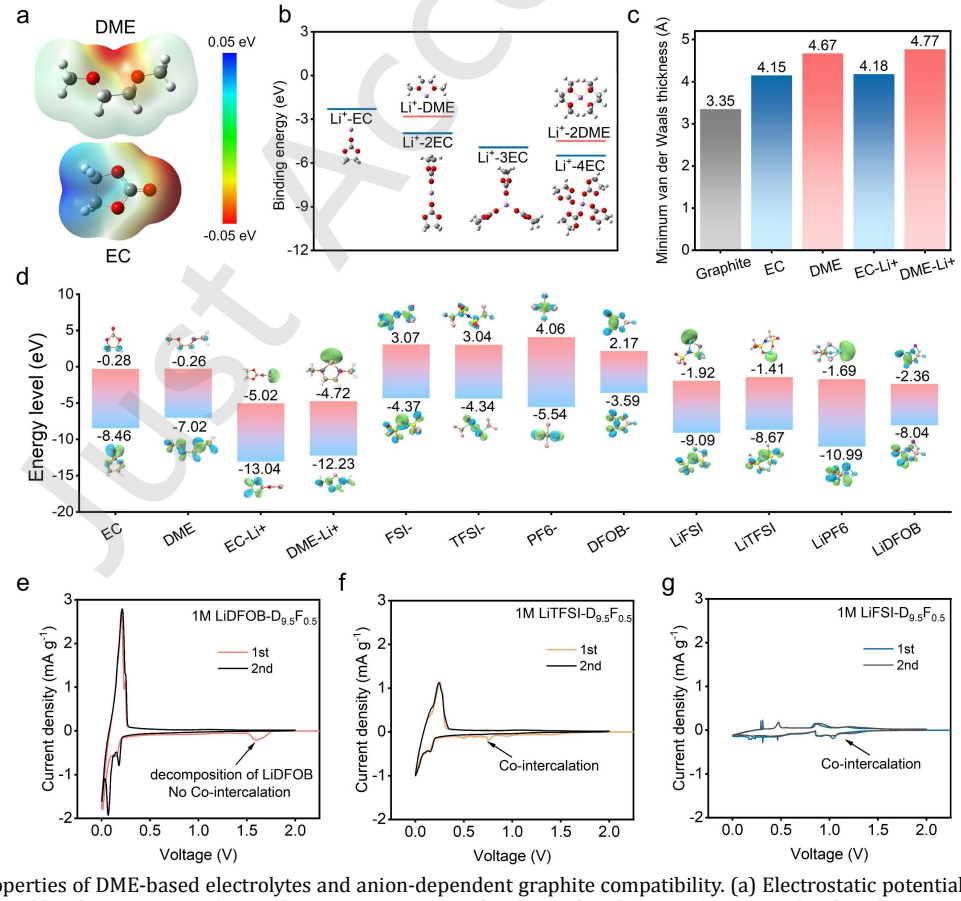


Figure 2. Molecular properties of DME-based electrolytes and anion-dependent graphite compatibility. (a) Electrostatic potential (ESP) distributions of DME and EC. (b) Calculated binding energies of Li^+ with one or two DME molecules and with one to four EC molecules; the comparison is made at equal numbers of coordinating oxygen atoms (1 DME = 2 O versus 2 EC = 2 O; 2 DME = 4 O versus 4 EC = 4 O). (c) Comparison of the graphite interlayer spacing with the calculated minimum van der Waals thicknesses of EC, DME, and their corresponding Li^+–solvent complexes. (d) Frontier molecular orbital energy levels of representative electrolyte components and their Li^+-coordinated species. (e–g) Initial cyclic voltammetry profiles of graphite in 1 M LiDFOB-$D_{9.5}F_{0.5}$, 1 M LiTFSI-$D_{9.5}F_{0.5}$, and 1 M LiFSI-$D_{9.5}F_{0.5}$ electrolytes, respectively

Just Accepted

These considerations define two coupled requirements for effective electrolyte design in DME-based systems: reducing the population of DME-associated Li^+ complexes reaching the graphite interface through solvation regulation, while promoting favorable interfacial reactions to suppress irreversible solvent co-intercalation. To decouple the influence of anion chemistry, three 1 M electrolytes were prepared in DME/FEC (95/5, v/v), denoted as 1 M LiDFOB-$D_{9.5}F_{0.5}$, 1 M LiTFSI-$D_{9.5}F_{0.5}$, and 1 M LiFSI-$D_{9.5}F_{0.5}$, respectively. Here, $D_{9.5}F_{0.5}$ represents the DME/FEC volume ratio of 95/5. $LiPF_6$ was excluded because insoluble $Li(DME)_2PF_6$ solvate crystals formed under the same DME-rich conditions (Figure S1), preventing a reliable comparison under homogeneous 1 M electrolyte conditions.

The intrinsic interaction between Li^+ and anions was first evaluated through pairwise binding-energy calculations (Figure S2). The calculated binding energies are −6.07, −5.93, and −5.79 eV for LiTFSI, LiDFOB, and LiFSI, respectively, corresponding to a Li^+–anion binding strength order of LiTFSI > LiDFOB > LiFSI. Although LiTFSI exhibits the strongest binding, it does not provide the best graphite compatibility, indicating that pairwise Li^+–anion binding strength alone is insufficient to explain the electrolyte-dependent graphite behavior. Instead, effective solvation regulation requires consideration of not only Li+–anion interaction strength but also the ability of anions to participate in Li+ solvation, their interfacial reduction behavior, and the structural accessibility of the resulting solvation complexes. Although stronger anion binding may facilitate anion participation within Li^+ solvation structures, excessive stabilization of ion pairs does not necessarily translate into improved interfacial behavior. Therefore, an appropriate balance between anion participation and interfacial reactivity is required to regulate both solvation structures and electrode/electrolyte reactions.

Beyond Li^+–anion interactions, the intrinsic electronic properties of different anions were further investigated through frontier molecular orbital calculations (Figure 2d). $DFOB^-$ exhibits a lower LUMO energy (2.17 eV) compared with FSI^- (3.07 eV) and $TFSI^-$ (3.04 eV). After Li^+ coordination, the LUMO energy of LiDFOB decreases to −2.36 eV, lower than those of LiFSI (−1.92 eV) and LiTFSI (−1.41 eV). The relatively lower LUMO level suggests that DFOB-containing species possess a higher tendency to participate in early electron-transfer processes at the electrode/electrolyte interface. However, considering that LUMO energies alone cannot directly determine the actual decomposition pathways in complex electrolyte environments, these calculations mainly provide an electronic descriptor for comparing the relative reduction tendency of different anion-derived species. The influence of anion chemistry on graphite compatibility is reflected in the initial electrochemical responses (Figures 2e–g). The 1 M LiDFOB-$D_{9.5}F_{0.5}$ electrolyte exhibits a distinct cathodic feature at 1.5–1.7 V only during the first scan, followed by well-defined graphite lithiation/delithiation features in subsequent cycles. In comparison, the 1 M LiTFSI-$D_{9.5}F_{0.5}$ electrolyte shows a pronounced cathodic process during the first cycle, which gradually decreases after additional cycling as graphite redox behavior develops. The 1 M LiFSI-$D_{9.5}F_{0.5}$ electrolyte displays persistent parasitic cathodic features accompanied by incomplete graphite lithiation responses. These distinct CV evolution behaviors indicate different initial interfacial reaction behaviors induced by the three anions, with LiDFOB-$D_{9.5}F_{0.5}$ providing the most favorable initial interfacial environment for reversible graphite lithiation.

To test whether this behavior is specific to $DFOB^-$ or a more general property of boron-containing anions, two additional electrolytes were prepared with the same solvent composition and nominal salt concentration, 1 M LiBOB-$D_{9.5}F_{0.5}$ and 1 M LiBF4-$D_{9.5}F_{0.5}$ (Figure S3). LiBOB shares the oxalate ligand of $DFOB^-$ and reproduces the key features: the reduction current above 0.4 V remains small, and a lithiation/delithiation couple develops at 0.2–0.3 V. LiBF4, which contains no oxalate group, instead shows a weak but persistent cathodic current between 0.5 and 1.2 V and no resolved staging features, consistent with continuous solvent reduction rather than the formation of a protective interphase. The beneficial effect therefore requires the oxalate ligand rather than boron alone.

The distinct graphite responses of 1 M LiDFOB-$D_{9.5}F_{0.5}$, 1 M LiTFSI-$D_{9.5}F_{0.5}$, and 1 M LiFSI-$D_{9.5}F_{0.5}$ indicate that interfacial stabilization alone cannot fully determine graphite compatibility. Therefore, the local Li^+ solvation environment was further investigated to clarify how anion chemistry regulates the accessibility of DME-involved Li^+ coordination structures during graphite lithiation. Molecular dynamics simulations were performed to resolve the coordination structures between Li^+ and different electrolyte components [14]. The radial distribution functions (RDFs) and corresponding coordination-number profiles (Figures 3a, b) reveal distinct primary solvation structures among the three electrolytes.

Among the three electrolytes, 1 M LiDFOB-$D_{9.5}F_{0.5}$ exhibits a distinct solvation preference characterized by enhanced $DFOB^-$ participation and reduced Li^+–DME coordination within the primary solvation sheath. In contrast, 1 M LiTFSI-$D_{9.5}F_{0.5}$ and 1 M LiFSI-$D_{9.5}F_{0.5}$ maintain higher Li^+–DME coordination numbers, indicating a larger fraction of DME-involved Li^+ coordination structures. These results suggest that $DFOB^-$ effectively competes with DME for Li^+ coordination and shifts the local solvation structure toward anion-involved configurations rather than DME-dominated environments. Component-resolved RDF analysis further indicates that FEC contributes only marginally to the differences in the primary solvation structures among the three electrolytes (Figure S4), suggesting that the altered coordination preference mainly originates from the competition between DME and anions for Li^+ coordination.

The reduced DME involvement revealed by molecular dynamics simulations is further supported by Raman spectroscopy (Figure 3c). Compared with 1 M LiTFSI-$D_{9.5}F_{0.5}$ and 1 M LiFSI-$D_{9.5}F_{0.5}$, the Li^+-coordinated DME vibration band near 875 cm^{-1} is significantly weakened in 1 M LiDFOB-$D_{9.5}F_{0.5}$, whereas the contribution from free DME around 849 cm^{-1} becomes relatively enhanced. These spectral variations are consistent with the MD results, demonstrating that

Just Accepted

DFOB⁻ participation decreases the fraction of DME-involved Li^+ coordination structures. The reduced contribution of DME to Li^+ coordination may help suppress solvent co-intercalation in conjunction with the protective interphase formed during initial lithiation.

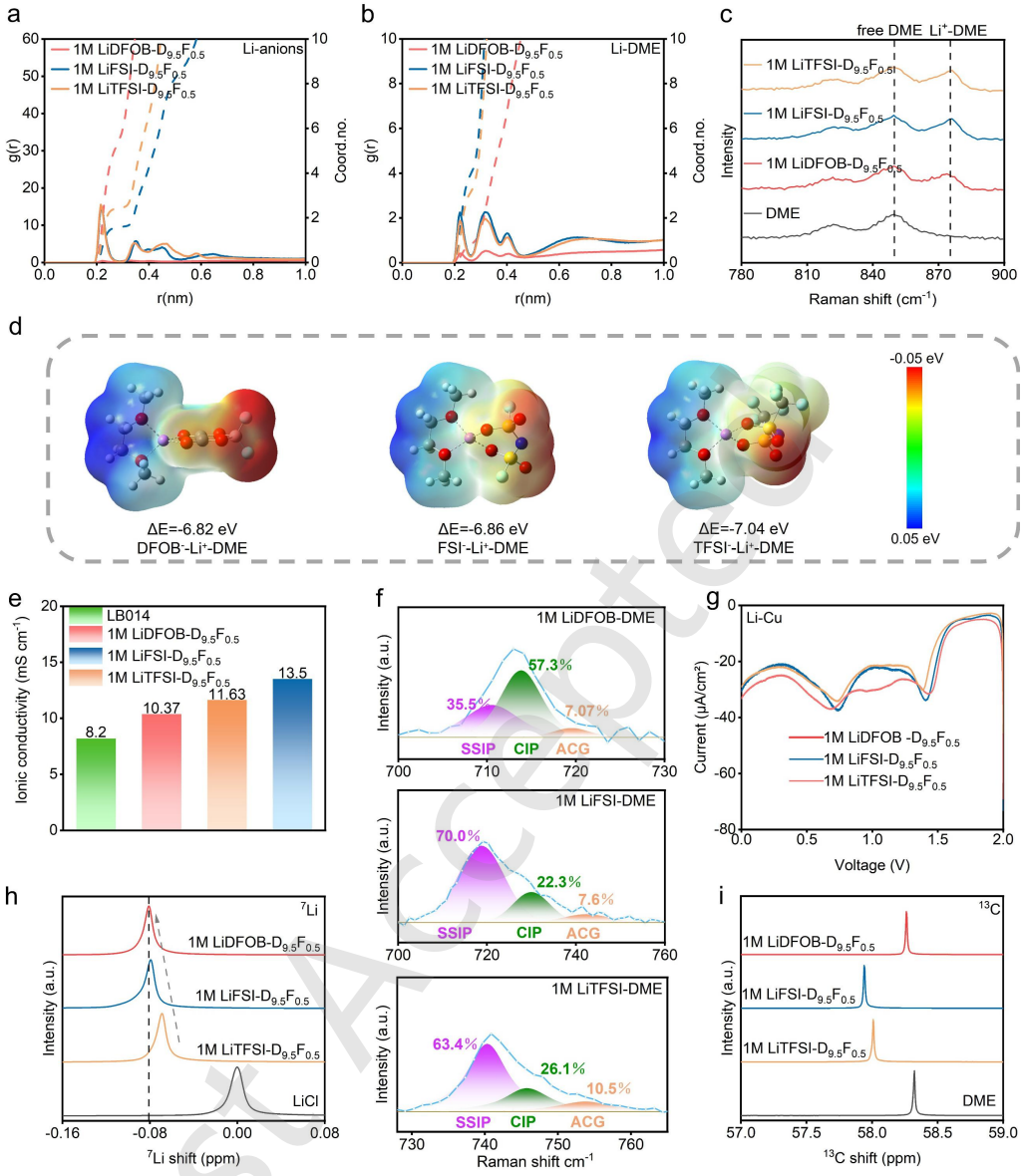


Figure 3. Solvation structures, ion association, and interfacial reduction behavior of DME-based electrolytes. (a) Li^+–anion radial distribution functions (RDFs) and corresponding coordination numbers. (b) Li^+–DME RDFs and corresponding coordination numbers. (c) Raman spectra in the DME coordination region for different electrolytes and pristine DME. (d) Calculated interaction energies and electrostatic potential distributions of representative $DFOB^-$–Li^+–DME, FSI^-–Li^+–DME, and $TFSI^-$–Li^+–DME configurations. (e) Ionic conductivities of different electrolytes. (f) Raman deconvolution of anion association states, including solvent-separated ion pairs (SSIPs), contact ion pairs (CIPs), and aggregates (AGGs). (g) Initial cathodic responses of different electrolytes measured in Li||Cu cells. (h) ^7Li NMR spectra of different electrolytes with LiCl as the reference. (i) ^{13}C NMR spectra of different electrolytes and pristine DME.

Representative Li^+–anion–DME configurations were extracted from MD trajectories to examine their interaction energies and electrostatic potential distributions (Figure 3d). The calculated interaction energies are −6.82, −6.86, and −7.04 eV for $DFOB^-$–Li^+–DME, FSI^-–Li^+–DME, and $TFSI^-$–Li^+–DME, respectively. These three values span only 0.22 eV, within the uncertainty of the method, and are therefore reported for completeness rather than used to rank the anions or to rationalize the extent of their participation in the primary sheath. These energies describe the overall interactions within the ternary complexes and do not independently quantify DME dissociation energies. Together with the reduced DME coordination revealed by MD simulations and Raman spectroscopy, these results support the role of anion identity in modifying the structural and energetic characteristics of the Li^+ coordination environment. The comparison also resolves the apparent inconsistency between the pairwise binding energies and the involvement of the anions in the primary sheath. The pairwise values were obtained in the gas phase for isolated ion pairs, and they describe the intrinsic Li^+–anion affinity rather than the free-energy change of exchanging a DME molecule for an anion in an explicitly solvated environment where about nine DME molecules compete for each Li^+. A gas-phase pairwise energy is a local property of the dimer: it says nothing about how the anion packs against the surrounding

Just Accepted

solvent or how much solvent volume it displaces, and it is this packing term that decides the composition of the sheath in the electrolyte. In addition, $DFOB^-$ chelates Li^+ through its two oxalate oxygen atoms and therefore occupies two coordination sites per bound anion, so that it displaces more DME than an anion coordinating through a single oxygen. Together with the chelating coordination of $DFOB^-$, these two factors explain why the anion with the weakest pairwise binding is the most strongly involved in the primary sheath.

Importantly, the reconstructed solvation environment does not compromise Li^+ transport kinetics. The 1 M LiDFOB-$D_{9.5}F_{0.5}$ electrolyte exhibits an ionic conductivity of 10.37 mS cm^{-1} (Figure 3e), comparable to those of the 1 M LiTFSI-$D_{9.5}F_{0.5}$ and 1 M LiFSI-$D_{9.5}F_{0.5}$ electrolytes and higher than that of the conventional EC-based electrolyte (LB014, 1 M $LiPF_6$/EC-DEC-EMC, 1:1:1; 8.20 mS cm^{-1}). More importantly, potentiostatic polarization combined with EIS measurements (Figure S5) reveal a higher Li^+ transference number (t^+ = 0.71) for 1 M LiDFOB-$D_{9.5}F_{0.5}$, compared with 1 M LiTFSI-$D_{9.5}F_{0.5}$ (0.53) and 1 M LiFSI-$D_{9.5}F_{0.5}$ (0.47). Consequently, the Li^+-carried conductivity (σtLi^+) reaches 7.36 mS cm^{-1}, exceeding those of 1 M LiTFSI-$D_{9.5}F_{0.5}$ (6.16 mS cm^{-1}) and 1 M LiFSI-$D_{9.5}F_{0.5}$ (6.35 mS cm^{-1}). These results demonstrate that $DFOB^-$-regulated solvation decreases DME involvement while increasing the contribution of Li^+ migration to ionic conduction, providing favorable kinetic conditions for fast-charging graphite.

The altered solvation environment is further reflected in the distribution of ionic association states. Anion-related Raman deconvolution (Figure 3f) reveals distinct ion-pairing characteristics among the three electrolytes. The 1 M LiDFOB-$D_{9.5}F_{0.5}$ electrolyte exhibits a higher fraction of contact ion pairs (CIPs, 57.3%) with limited aggregated ion pairs (AGG) formation (7.07%), whereas 1 M LiTFSI-$D_{9.5}F_{0.5}$ and 1 M LiFSI-$D_{9.5}F_{0.5}$ electrolytes show lower CIP fractions (26.1% and 22.3%, respectively) accompanied by larger contributions from solvent-separated ion pairs (SSIPs). The coexistence of abundant CIPs and limited AGGs in 1 M LiDFOB-$D_{9.5}F_{0.5}$ indicates enhanced anion participation without inducing excessive ionic clustering. Such a balanced ionic association state maintains Li^+ transport efficiency while increasing the probability of anion-derived species participating in interfacial reactions.

The preferential interfacial reaction of anion-derived species was further evaluated using Li||Cu cells (Figure 3g). Compared with 1 M LiTFSI-$D_{9.5}F_{0.5}$ and 1 M LiFSI-$D_{9.5}F_{0.5}$, the 1 M LiDFOB-$D_{9.5}F_{0.5}$ electrolyte exhibits an earlier cathodic response over a broader potential range, indicating preferential activation of DFOB-derived species during the initial reduction process. This behavior is consistent with the enhanced electronic accessibility of LiDFOB-related species revealed by frontier orbital analysis and the increased anion participation observed from Raman analysis. Importantly, the Li||Cu response does not directly determine the final interfacial composition; rather, it demonstrates that DFOB-derived species can participate in the initial reduction process before extensive solvent decomposition occurs. Combined with the graphite CV results, these observations suggest that 1 M LiDFOB-$D_{9.5}F_{0.5}$ promotes an early anion-involved interfacial reaction pathway, thereby suppressing solvent-driven side reactions and improving graphite compatibility.

To clarify the respective contributions of $DFOB^-$ and FEC, a control electrolyte containing 1 M LiDFOB in neat DME (1 M LiDFOB-D10) was additionally evaluated (Figure S6). Although $DFOB^-$ is present in the solvation environment, the LiDFOB-D10 electrolyte still exhibits pronounced solvent-related cathodic features during the initial lithiation process, suggesting that $DFOB^-$-mediated solvation regulation alone is insufficient to fully eliminate DME-associated interfacial reactions. Conversely, the LiTFSI and LiFSI electrolytes contain the same 5 vol% FEC yet fail to stabilize graphite (Figures 2e–g), so interfacial stabilization by FEC alone is also insufficient. Therefore, the improved graphite compatibility of LiDFOB-$D_{9.5}F_{0.5}$ originates from the synergistic contribution of $DFOB^-$-regulated solvation and FEC-assisted interfacial regulation, which operate at different levels: $DFOB^-$ reduces the population of DME-rich solvation structures reaching the interface, whereas FEC supplies the early LiF-forming reaction that $DFOB^-$ alone does not deliver at a sufficient rate. The FEC-free electrolyte exhibits an ionic conductivity of 13.0 mS cm^{-1} and a Li^+ transference number of 0.61, compared with 10.37 mS cm^{-1} and 0.71 for 1 M LiDFOB-$D_{9.5}F_{0.5}$ (Figure S6b, c). The 5 vol% FEC therefore lowers the Li^+-carried conductivity only from 7.9 to 7.36 mS cm^{-1}, while being indispensable for the interfacial stability described above.

To determine the FEC content required for this stabilization, electrolytes containing 2 and 10 vol% FEC were examined under identical conditions (Figure S7). At 2 vol%, no resolved graphite lithiation/delithiation peaks develop in the 0.1–0.3 V region and a distinct feature persists at about 0.43 V, indicating that the interface is not yet stabilized. At 10 vol%, well-resolved peaks appear at about 0.10 and 0.20 V, comparable to those observed for the 5 vol% formulation described above. The 5 vol% level is therefore the lowest FEC content that establishes a reversible graphite interface, and increasing the content to 10 vol% brings no further interfacial benefit.

The salt-dependent Li^+ solvation environments were further examined by NMR spectroscopy (Figures 3h, i). The ^7Li spectra exhibit distinct chemical-shift variations among the three electrolytes relative to the LiCl reference, with 1 M LiDFOB-$D_{9.5}F_{0.5}$ showing the largest deviation. This difference reflects a distinct time-averaged electronic environment around Li^+ and provides complementary experimental evidence for the modified solvation structure revealed by MD simulations. The solvent-side response obtained from ^{13}C NMR further probes the perturbation of DME molecules. Compared with 1 M LiFSI-$D_{9.5}F_{0.5}$ and 1 M LiTFSI-$D_{9.5}F_{0.5}$, the DME resonance in 1 M LiDFOB-$D_{9.5}F_{0.5}$ remains closer to that of pristine DME, indicating weaker average perturbation of the DME chemical environment. Similar behavior is observed in the ^1H NMR spectra (Figure S8), where 1 M LiDFOB-$D_{9.5}F_{0.5}$ induces the smallest chemical-shift variation of DME signals. Together with MD simulations and Raman spectroscopy, these NMR results further verify that $DFOB^-$ reshapes the Li^+ solvation environment by reducing persistent DME-involved coordination structures while introducing anion participation.

Under Review

Collectively, these results establish a coupled solvation–interfacial regulation mechanism enabled by 1 M LiDFOB-$D_{9.5}F_{0.5}$. Rather than simply strengthening Li^+–anion interactions or inducing extensive electrolyte decomposition, $DFOB^-$ reconstructs the Li^+ solvation environment by competing with DME for coordination and simultaneously facilitates early anion-involved interfacial reactions. In the electrolyte phase, this regulation decreases the fraction of DME-associated Li^+ species approaching the graphite surface while maintaining efficient Li^+ transport. At the interface, preferential participation of DFOB-derived species enables a more favorable interfacial environment before sustained solvent-driven reactions occur. The synchronization between solvation-shell regulation and interfacial reaction control allows DME electrolytes to retain their intrinsic fast-transport advantage while overcoming their inherent graphite incompatibility, providing the fundamental basis for high-rate graphite operation.

The high-rate cycling performance of graphite was first evaluated in Gr||Li half-cells at 5 C within 0.01–1.5 V (Figure 4a). After an initial activation process, the 1 M LiDFOB-$D_{9.5}F_{0.5}$ electrolyte exhibits a gradual increase in reversible capacity, which stabilizes above 320 mAh g^{-1} and reaches approximately 325 mAh g^{-1} during subsequent cycling. Even after nearly 300 cycles, the cell maintains a reversible capacity of approximately 303 mAh g^{-1}. In comparison, the conventional carbonate electrolyte LB014 delivers only approximately 255 mAh g^{-1} after 300 cycles, whereas 1 M LiTFSI-$D_{9.5}F_{0.5}$ and 1 M LiFSI-$D_{9.5}F_{0.5}$ retain only ~114 and ~96 mAh g^{-1}, respectively.

The origin of the distinct initial electrochemical behaviors is further illustrated by the first-cycle galvanostatic voltage profiles (Figure S9). The 1 M LiDFOB-$D_{9.5}F_{0.5}$ electrolyte exhibits a pronounced plateau at approximately 1.6 V during the initial lithiation, corresponding to the cathodic feature observed in CV and suggesting an initial interfacial reaction prior to low-potential graphite lithiation. In contrast, 1 M LiFSI-$D_{9.5}F_{0.5}$ and 1 M LiTFSI-$D_{9.5}F_{0.5}$ exhibit more gradual high-voltage profiles without a comparable plateau and deliver substantially lower reversible capacities. Notably, 1 M LiDFOB-$D_{9.5}F_{0.5}$ also achieves the highest initial Coulombic efficiency among the four electrolytes (71.27%), which rapidly increases to 97.68% in the second cycle and exceeds 99% within the first five cycles. These results indicate that the LiDFOB-based electrolyte enables rapid establishment of a highly reversible graphite interface, thereby reducing irreversible reactions during subsequent cycling.

The distinct electrochemical behaviors are further reflected in the structural evolution of graphite after the first cycle (Figure 4b). The graphite (002) reflection is largely preserved after the first cycle in the 1 M LiDFOB-$D_{9.5}F_{0.5}$ electrolyte, retaining 94.8% of its relative intensity compared with pristine graphite. In contrast, the corresponding (002) reflections in 1 M LiTFSI-$D_{9.5}F_{0.5}$ and 1 M LiFSI-$D_{9.5}F_{0.5}$ decrease markedly to 45.0% and 39.3%, respectively, indicating substantial disruption of the ordered graphite stacking structure. Notably, no stable low-angle crystalline phase associated with persistent co-intercalation products is observed after cycling, suggesting that the electrochemical side reactions do not evolve into long-lived crystalline interlayer structures. Instead, the attenuation of the graphite (002) reflection in 1 M LiTFSI-$D_{9.5}F_{0.5}$ and 1 M LiFSI-$D_{9.5}F_{0.5}$ indicates irreversible deterioration of graphitic ordering, whereas 1 M LiDFOB-$D_{9.5}F_{0.5}$ effectively preserves the structural integrity of graphite during electrochemical activation.

The rate capability of graphite was subsequently evaluated under progressively increased current densities (Figure 4c). At moderate rates of 0.5–2 C, 1 M LiDFOB-$D_{9.5}F_{0.5}$ and the conventional carbonate electrolyte LB014 exhibit comparable capacities, with LB014 showing slightly higher values. However, their performance gradually diverges under more demanding high-rate conditions. The 1 M LiDFOB-$D_{9.5}F_{0.5}$ electrolyte maintains reversible capacities of approximately 320, 307, and 290 mAh g^{-1} at 3, 4, and 5 C, respectively, whereas LB014 decreases to approximately 317, 289, and 256 mAh g^{-1}. The difference becomes much more pronounced for the other DME-based electrolytes, with 1 M LiTFSI-$D_{9.5}F_{0.5}$ and 1 M LiFSI-$D_{9.5}F_{0.5}$ delivering only ~129 and ~106 mAh g^{-1} at 5 C, respectively. When the current rate is returned to 1 C, the 1 M LiDFOB-$D_{9.5}F_{0.5}$ cell rapidly recovers to approximately 352 mAh g^{-1}, demonstrating highly reversible rate performance.

The normalized capacity retention further highlights the high-rate capability of the 1 M LiDFOB-$D_{9.5}F_{0.5}$ electrolyte (Figure 4d). Relative to the capacity at 0.5 C, the cell retains approximately 96%, 87%, and 79% of its capacity at 1, 3, and 5 C, respectively, whereas LB014 exhibits a larger capacity loss and retains only ~67% at 5 C. Consistently, the galvanostatic voltage profiles of the 1 M LiDFOB-$D_{9.5}F_{0.5}$ cell preserve the characteristic graphite lithiation/delithiation features throughout the 0.5–5 C range despite increased polarization (Figure 4e). In contrast, 1 M LiFSI-$D_{9.5}F_{0.5}$ and 1 M LiTFSI-$D_{9.5}F_{0.5}$ show progressively enlarged polarization and pronounced capacity contraction with increasing rate (Figure S10). These results demonstrate that the LiDFOB-regulated electrolyte environment enables rapid and reversible graphite lithiation/delithiation under high-rate conditions.

The kinetic characteristics of the graphite/electrolyte interface were further evaluated by electrochemical impedance spectroscopy (Figure 4f). Although the uncycled cells already exhibit electrolyte-dependent impedance responses (Figure S11), the differences become more evident after the initial electrochemical activation. The 1 M LiDFOB-$D_{9.5}F_{0.5}$ electrolyte exhibits a moderate impedance response with relatively continuous evolution toward the low-frequency transport region, whereas 1 M LiFSI-$D_{9.5}F_{0.5}$ and 1 M LiTFSI-$D_{9.5}F_{0.5}$ display an additional low-frequency semicircular feature, indicating distinct interfacial relaxation behaviors. In comparison, the conventional carbonate electrolyte LB014 exhibits a larger overall impedance, consistent with its stable graphite compatibility but relatively slower interfacial kinetics.

Just Accepted

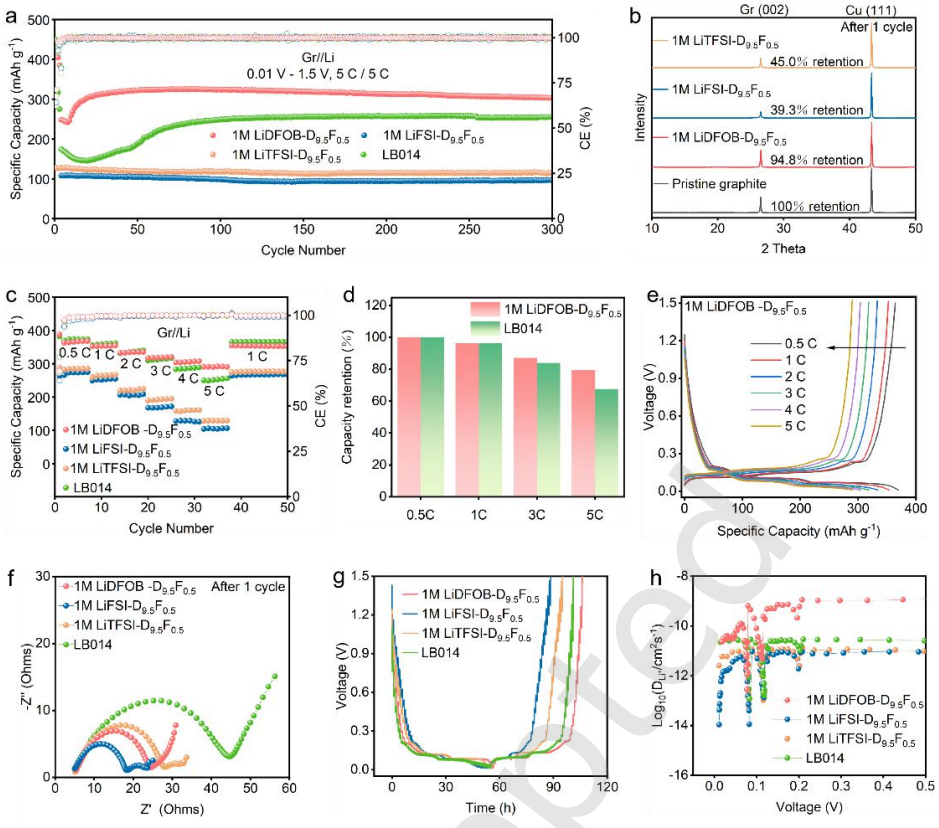


Figure 4. High-rate electrochemical performance and Li^+ transport kinetics of graphite anodes in different electrolytes. (a) Long-term cycling performance of Gr||Li cells at 5 C. (b) *Ex situ* XRD patterns of pristine graphite and graphite electrodes after the first cycle in different electrolytes. (c) Rate performance of graphite anodes from 0.5 to 5 C. (d) Normalized capacity retention of graphite in 1 M LiDFOB-$D_{9.5}F_{0.5}$ and LB014 at different C-rates. (e) Galvanostatic voltage profiles of graphite in 1 M LiDFOB-$D_{9.5}F_{0.5}$ at different C-rates. (f) EIS spectra of graphite electrodes after the first cycle. (g) GITT voltage responses of graphite in different electrolytes. (h) Corresponding apparent Li^+ diffusion coefficients derived from GITT measurements

Interestingly, 1 M LiFSI-$D_{9.5}F_{0.5}$ exhibits an even smaller apparent impedance than 1 M LiDFOB-$D_{9.5}F_{0.5}$ after the first cycle, yet delivers substantially inferior high-rate capacity. This comparison indicates that graphite rate performance is not simply determined by minimizing interfacial impedance. Instead, the electrochemical behavior depends on the balance between sufficient interfacial stabilization and efficient Li^+ transport. The 1 M LiDFOB-$D_{9.5}F_{0.5}$ electrolyte achieves this balance, enabling rapid Li^+ transfer while maintaining reversible graphite lithiation/delithiation.

The kinetics of graphite lithiation and delithiation were further evaluated using the galvanostatic intermittent titration technique (GITT) (Figures 4g, h) [39]. All four electrolytes exhibit pulse–relaxation voltage responses, while the calculated apparent Li^+ diffusion coefficients vary considerably with potential and show pronounced decreases in the low-potential region. At higher potentials, the apparent diffusion coefficient for 1 M LiDFOB-$D_{9.5}F_{0.5}$ reaches approximately 10^{-9} cm^2 s^{-1}, whereas those for 1 M LiFSI-$D_{9.5}F_{0.5}$, 1 M LiTFSI-$D_{9.5}F_{0.5}$, and LB014 predominantly remain on the order of 10^{-11} cm^2 s^{-1} in the same region. These results indicate more favorable apparent Li^+ transport kinetics in the LiDFOB-based system under the applied measurement conditions, consistent with its superior rate performance.

A representative enlarged GITT segment further reveals that the 1 M LiDFOB-$D_{9.5}F_{0.5}$ electrolyte exhibits a pulse polarization of 8.1 mV, comparable to 1 M LiFSI-$D_{9.5}F_{0.5}$ (8.0 mV) and 1 M LiTFSI-$D_{9.5}F_{0.5}$ (5.1 mV), while significantly lower than LB014 (17.3 mV) (Figure S12). Combined with the impedance results, these observations demonstrate that the LiDFOB-regulated electrolyte environment facilitates efficient interfacial Li^+ transfer and rapid Li^+ redistribution within graphite. Therefore, the superior high-rate performance of 1 M LiDFOB-$D_{9.5}F_{0.5}$ originates from the synergistic optimization of interfacial stability and Li^+ transport kinetics rather than from minimizing a single kinetic parameter. The comparable pulse polarizations of the LiFSI and LiDFOB electrolytes are likewise not inconsistent with their very different capacity retention, because the two measurements probe different quantities: the impedance semicircle reflects the ionic and charge-transfer resistance of the interphase at the time of measurement, whereas the pulse polarization of a single GITT step reflects the instantaneous ohmic and diffusion polarization. Neither integrates the cumulative Coulombic loss caused by continuous electrolyte reduction. An interphase that is thin and ionically conductive but chemically permeable therefore gives a small impedance and an unremarkable pulse polarization, while still allowing DME and FSI^- to reach the graphite edge planes throughout cycling, consistent with the persistent parasitic current in the first-cycle CV (Figure 2g) and with the continuous capacity decay in Figure 4a. Consistently, the LiFSI electrolyte shows the lowest capacity of the three after 300 cycles despite a pulse polarization essentially identical to that of LiDFOB, and the LiTFSI electrolyte, with the smallest pulse polarization (5.1 mV),

Just Accepted

also degrades faster than LiDFOB; the pulse polarization therefore does not order the capacity retention. To understand how different electrolyte chemistries affect the structural evolution of graphite during the initial cycling process, scanning electron microscopy (SEM) was performed on graphite electrodes after the first cycle. At the 10 μm scale (Figure S13), the graphite electrode cycled in 1 M LiDFOB-$D_{9.5}F_{0.5}$ largely preserves the well-defined platelet morphology, clear particle boundaries, and layered structure of pristine graphite, indicating limited structural disruption during the initial electrochemical process. In contrast, graphite cycled in 1 M LiTFSI-$D_{9.5}F_{0.5}$ exhibits increased surface roughening and irregular surface features, whereas 1 M LiFSI-$D_{9.5}F_{0.5}$ leaves a markedly different morphology, in which the originally compact platelets are opened into thin, delaminated flakes with split edges and abundant fractured fragments.

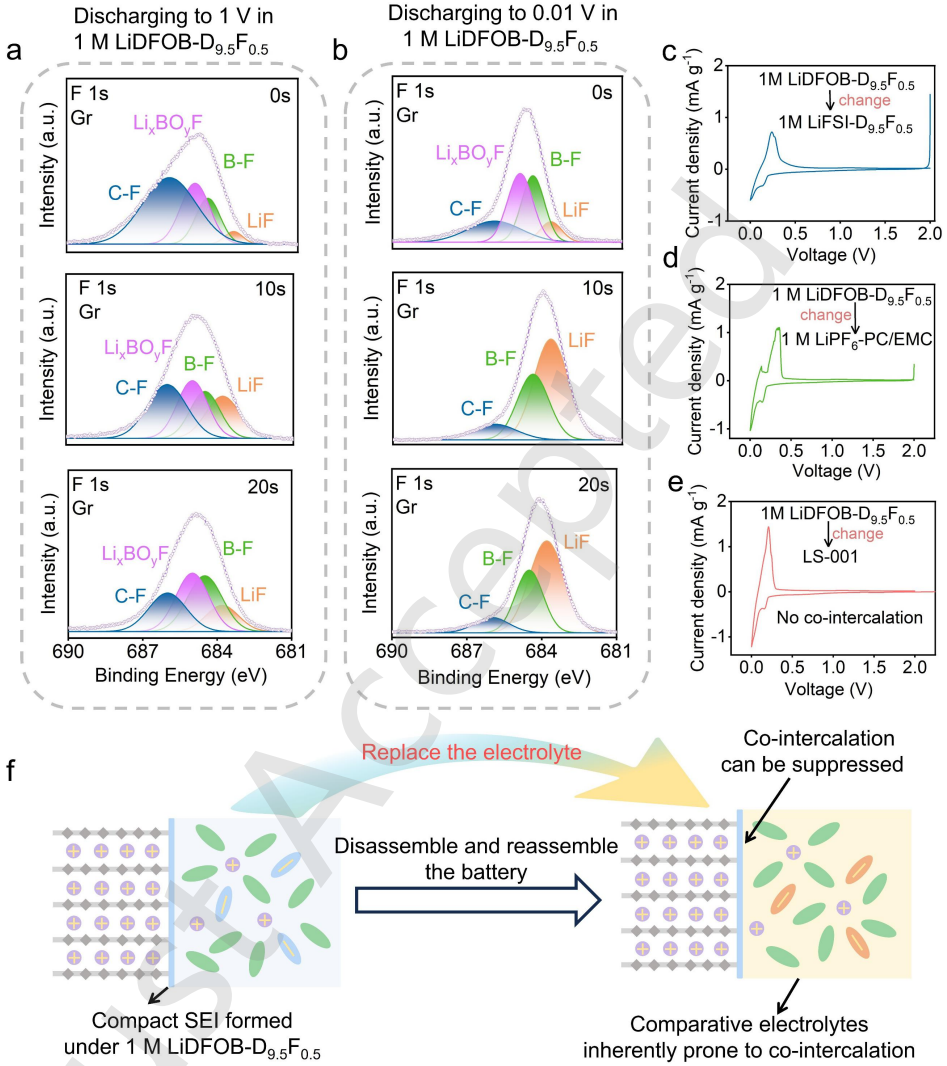


Figure 5. LiDFOB-derived interphase enabling persistent suppression of solvent co-intercalation in graphite. (a, b) F 1s XPS depth profiles of graphite anodes collected at 1.0 and 0.01 V, respectively, during initial lithiation in 1 M LiDFOB-$D_{9.5}F_{0.5}$. (c–e) Cyclic voltammetry responses of LiDFOB-derived SEI-protected graphite electrodes after replacing the electrolyte with 1 M LiFSI-$D_{9.5}F_{0.5}$, 1 M $LiPF_6$-PC/EMC, and LS-001 (1 M LiTFSI in 1,3-dioxolane/DME, 1:1, v/v) electrolyte, respectively. (f) Schematic illustration of the persistent protection mechanism of LiDFOB-derived SEI against solvent co-intercalation after electrolyte replacement

At higher magnification (2 μm scale, Figure S14), these differences become more apparent. The graphite electrode from 1 M LiDFOB-$D_{9.5}F_{0.5}$ maintains a relatively uniform surface morphology while preserving the underlying lamellar framework. In comparison, 1 M LiTFSI-$D_{9.5}F_{0.5}$ results in abundant granular features distributed across the graphite surface, suggesting a more heterogeneous surface evolution. The graphite electrode cycled in 1 M LiFSI-$D_{9.5}F_{0.5}$ exhibits more disrupted platelet edges and locally loosened structures, indicating stronger structural perturbation during cycling. A larger-field SEM image (50 μm scale, Figure S15) further reveals apparent layer separation and exfoliation features for the LiFSI-cycled graphite, whereas the LiDFOB-cycled electrode maintains a more intact particle distribution. These observations demonstrate that the LiDFOB-regulated electrolyte environment effectively preserves graphite structural integrity during the initial electrochemical process.

The distinct morphological evolution indicates that different electrolyte chemistries induce different interfacial reaction pathways. Therefore, the chemical composition and evolution of the graphite interfacial layer were further investigated by F 1s XPS depth profiling [40–43].

To track the potential-dependent evolution of the

Just Accepted

interfacial layer during initial lithiation, graphite electrodes harvested at 1.0 and 0.01 V were analyzed by F 1s XPS depth profiling (Figures 5a, b). At 1.0 V (Figure 5a), corresponding to the early stage of interfacial layer formation, the F 1s spectra show the coexistence of C–F, LiF, B–F, and $Li_xBO_yF_z$ species. The simultaneous appearance of organic and inorganic fluorinated components indicates that the interfacial layer is undergoing dynamic construction involving both solvent decomposition and the reduction of DFOB-derived species. Notably, B–F-containing species are already detectable at this relatively high potential, demonstrating the early participation of DFOB-derived species in interfacial formation. Meanwhile, the relatively limited LiF contribution suggests that the inorganic fluorinated components are still developing at this stage.

Upon further lithiation to 0.01 V (Figure 5b), the interfacial composition undergoes further evolution. Compared with the 1.0 V state, the LiF contribution becomes significantly enhanced, accompanied by a reduced relative contribution from C–F species. Meanwhile, B–F-containing species remain detectable throughout the sputtering process, indicating the continuous presence of DFOB-derived boron-containing fluorinated components within the interfacial layer. The simultaneous enrichment of LiF and boron-containing inorganic species suggests the gradual formation of an inorganic-rich interfacial structure during deep lithiation.

These results demonstrate that $DFOB^-$ derived species participate in the early construction of a chemically robust interfacial layer, which subsequently evolves toward a more inorganic-rich structure during lithiation. To further verify whether this pre-established interface, rather than the continuous presence of LiDFOB in the electrolyte, governs graphite compatibility, electrolyte replacement experiments were performed.

Graphite electrodes were first lithiated to 1.0 V in 1 M LiDFOB-$D_{9.5}F_{0.5}$, harvested, rinsed with DME, and transferred into 1 M LiFSI-$D_{9.5}F_{0.5}$, 1 M $LiPF_6$-PC/EMC (1:1, v/v), or LS-001 (1 M LiTFSI in 1,3-dioxolane/DME, 1:1, v/v) electrolytes for subsequent CV measurements (Figures 5c–e). After electrolyte replacement, the electrodes transferred to the LiFSI and LS-001 electrolytes exhibited reversible graphite lithiation/delithiation responses without evident cathodic features associated with solvent co-intercalation (Figures 5c and 5e). These results indicate that the interphase preformed in the LiDFOB electrolyte remains effective in maintaining graphite electrochemical reversibility in both ether-based replacement electrolytes. Figure 5f schematically illustrates this interfacial protection, whereby the preformed SEI suppresses solvent co-intercalation while allowing reversible Li^+ intercalation and deintercalation. These results highlight the importance of early interfacial passivation in establishing graphite compatibility. Galvanostatic cycling at 5 C confirmed that this protection is persistent: after replacement with 1 M LiFSI-$D_{9.5}F_{0.5}$ or LS-001, the cells recovered to approximately 235 and 222 mAh g^{-1} at the 50th cycle with Coulombic efficiencies close to 100% (Figure S16), whereas a cell cycled in 1 M LiFSI-$D_{9.5}F_{0.5}$ from the start degrades continuously (Figure 4a). For 1 M $LiPF_6$-PC/EMC, stable cycling was not achieved under the same conditions. To further evaluate the high-voltage compatibility of LiDFOB-regulated DME electrolytes, the anodic stability and interfacial behavior on high-voltage cathodes were investigated. Linear sweep voltammetry (LSV) measurements using Li||Al cells reveal distinct oxidative stability among different electrolytes (Figure 6a). The LiFSI-based electrolyte exhibits a sharp increase in anodic current above 4.1 V, indicating accelerated electrolyte oxidation at high potentials. In comparison, the LiDFOB-based electrolyte maintains a much lower oxidation current up to 5.0 V, suggesting suppressed oxidative decomposition and improved anodic stability.

The long-term oxidative stability was further examined through chronoamperometric measurements on Li||NCM811 cells held at 4.4 V (Figure 6b). Under continuous high-voltage polarization, the LiFSI electrolyte exhibits a gradually increasing leakage current, indicating sustained parasitic oxidation reactions at the cathode interface. In contrast, the LiDFOB electrolyte maintains a much lower and more stable current response, demonstrating reduced interfacial side reactions under high-voltage operation.

The reversible electrochemical behavior of NCM811 cathodes was further evaluated by cyclic voltammetry (Figure 6c). Both $LiDFOB^-$ and LiTFSI-based electrolytes exhibit similar redox characteristics associated with NCM811 charge compensation processes, confirming that LiDFOB does not hinder the intrinsic cathode redox activity. Meanwhile, the comparable peak positions and polarization indicate preserved reaction kinetics. These results demonstrate that LiDFOB-regulated DME electrolytes simultaneously provide graphite compatibility and stable high-voltage cathode operation.

The practical viability of 1 M LiDFOB-$D_{9.5}F_{0.5}$ was further evaluated in high-loading Gr||NCM811 full cells cycled between 2.5 and 4.4 V at 4 C/4 C (Figure 6d). With graphite and NCM811 loadings of 6.3 and 10.5 mg cm^{-2}, respectively (high-loading electrodes; see Section 1.3 of the Supplementary Material), the 1 M LiDFOB-$D_{9.5}F_{0.5}$ electrolyte exhibits markedly improved cycling stability, maintaining a reversible capacity of 126.4 mAh g^{-1} after 300 cycles, corresponding to a capacity retention of approximately 80.2%. In comparison, the conventional carbonate electrolyte LB014 undergoes continuous capacity decay and delivers only 79.7 mAh g^{-1} after 300 cycles. The 1 M LiTFSI-$D_{9.5}F_{0.5}$ electrolyte exhibits substantially accelerated degradation, with its reversible capacity decreasing below 30 mAh g^{-1} after approximately 230 cycles. More notably, the 1 M LiFSI-$D_{9.5}F_{0.5}$ electrolyte fails to sustain stable cycling under the 4.4 V full-cell condition.

The evolution of the full-cell voltage profiles during cycling was further examined (Figure 6e). The charge–discharge curves of the cell using 1 M LiDFOB-$D_{9.5}F_{0.5}$ retain their overall shape from the 5th to the 300th cycle, while the discharge curves progressively shorten, consistent with the gradual capacity decline observed in Figure 6d. These results indicate that the full cell maintains its characteristic charge–discharge behavior during extended cycling between 2.5 and 4.4 V at 4 C/4 C.

Beyond long-term cycling stability, the rate capability of

Just Accepted

the Gr||NCM811 full cells were further evaluated under progressively increased current densities (Figure 6f). The 1 M LiDFOB-$D_{9.5}F_{0.5}$ electrolyte exhibits a much smaller capacity decay when the rate increases from 0.5 to 5 C. Even at 5 C, the cell maintains approximately 160 mAh g^{-1}, whereas the LB014 electrolyte shows a more pronounced capacity decrease with increasing current density. When the current density is returned to 1 C, the LiDFOB-based cell rapidly recovers its initial capacity, demonstrating excellent electrochemical reversibility under variable-rate operation.

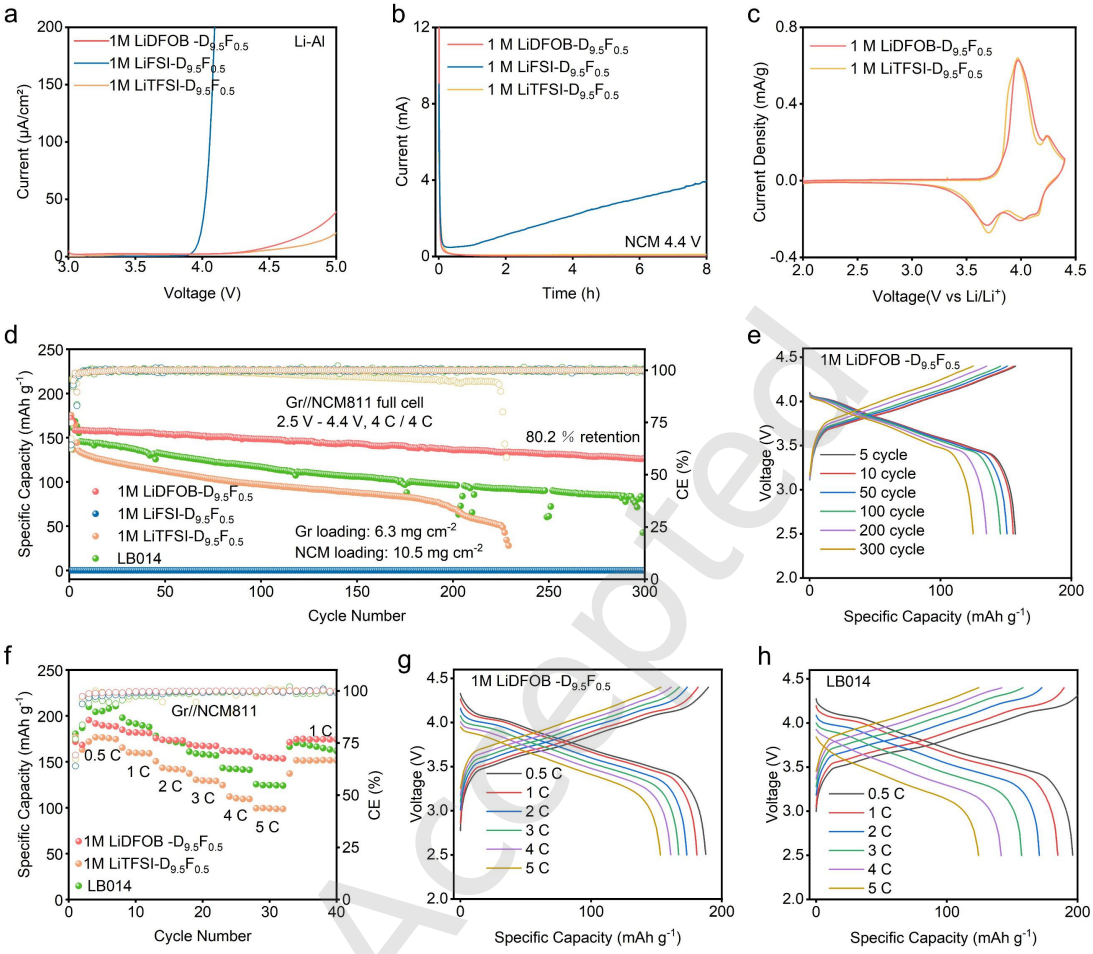


Figure 6. High-voltage compatibility and full-cell performance enabled by LiDFOB-regulated DME electrolyte. (a) Linear sweep voltammetry (LSV) curves of different electrolytes measured using Li||Al cells to evaluate anodic stability. (b) Chronoamperometric responses of different electrolytes in Li||NCM811 cells held at 4.4 V. (c) Cyclic voltammetry profiles of NCM811 electrodes in different electrolytes between 2.0 and 4.5 V. (d) Long-term cycling performance of Gr||NCM811 full cells using different electrolytes at 4 C with a voltage range of 2.5–4.4 V. The graphite and NCM811 loadings are 6.3 and 10.5 mg cm^{-2}, respectively. (e) Galvanostatic charge–discharge profiles of Gr||NCM811 full cells using 1 M LiDFOB-$D_{9.5}F_{0.5}$ electrolyte during long-term cycling. (f) Rate performance of Gr||NCM811 full cells using different electrolytes at current rates from 0.5 C to 5 C. (g, h) Galvanostatic charge–discharge profiles of Gr||NCM811 full cells using 1 M LiDFOB-$D_{9.5}F_{0.5}$ and LB014 electrolytes at different current rates, respectively.

The corresponding charge/discharge profiles further reveal the kinetic advantages of the LiDFOB electrolyte (Figures 6g, h). With increasing rate, the 1 M LiDFOB-$D_{9.5}F_{0.5}$ cell preserves relatively stable voltage profiles with moderate polarization growth, whereas the LB014 cell exhibits progressively enlarged voltage hysteresis and shortened charge/discharge plateaus, indicating increased kinetic limitations at high current densities. These results demonstrate that the LiDFOB-regulated interfacial chemistry not only improves long-term cycling stability but also enables efficient Li^+ transport under practical full-cell high-rate operation.

Overall, the high-loading Gr||NCM811 full-cell results demonstrate that the LiDFOB-regulated electrolyte strategy established in half-cell studies can be effectively extended to practical battery configurations. The improved cycling stability and high-rate capability originate from the stable graphite/electrolyte interface and favorable Li^+ transport kinetics enabled by LiDFOB regulation. These results highlight anion-mediated solvation and interphase engineering as an effective approach for developing high-power ether-based lithium-ion batteries.

3. Conclusion

In summary, a salt-mediated electrolyte strategy was developed to suppress solvent co-intercalation while preserving the rapid Li^+ transport characteristics of DME. In the 1 M LiDFOB-$D_{9.5}F_{0.5}$ electrolyte, $DFOB^-$ participates in the primary Li^+ solvation sheath and reduces the population of DME-involved coordination structures, as consistently supported by molecular dynamics simulations, Raman spectroscopy, and NMR measurements. This solvation regulation is coupled with early anion-involved interfacial reactions and FEC-assisted passivation, leading to the formation of a B-containing interphase that becomes progressively enriched in LiF during lithiation.

Un Accepted

Electrochemical measurements, *ex situ* XRD, SEM observations, and electrolyte-replacement experiments collectively demonstrate that the pre-established interphase effectively suppresses solvent-induced graphite degradation and enables reversible Li^+ intercalation. The resulting electrolyte retains a high ionic conductivity of 10.37 mS cm^{-1} and an apparent Li^+ transference number of 0.71, enabling graphite anodes to deliver approximately 325 mAh g^{-1} at 5 C and maintain approximately 303 mAh g^{-1} after nearly 300 cycles. Moreover, high-loading Gr||NCM811 full cells operated between 2.5 and 4.4 V at 4 C/4 C retain 126.4 mAh g^{-1} after 300 cycles, corresponding to a capacity retention of approximately 80.2%. These findings demonstrate that the graphite compatibility of DME-based electrolytes is governed by the coordinated regulation of bulk solvation and interfacial chemistry. For strongly coordinating ether-based electrolytes represented by DME, suppressing co-intercalation into the graphite anode while simultaneously achieving fast-charging performance generally requires the use of high-concentration or localized high-concentration electrolytes, which substantially increases the electrolyte cost. In contrast, the simple 1 M single-salt system employed in this work offers a pronounced cost advantage. The advantage lies in the salt inventory and in the simplicity of the formulation: a 1 M electrolyte consumes one third to one fifth of the salt required by the 3–5 M electrolytes used in high-concentration and localized high-concentration approaches, and it requires neither a fluorinated diluent nor a multi-component additive package. From a practical standpoint, the formulation is intended for near-ambient operation: a sample stored at 25 °C for two months retained its fast-charging capability (Figure S17a), whereas storage at 60 °C for three days increased the polarization and reduced the reversible capacity (Figure S17b), because accelerated $DFOB^-$ decomposition and FEC consumption thicken the interphase beyond its optimum. The electrolyte itself remained clear and colorless after the 60 °C storage, with no visible precipitate or phase separation (Figure S17c). This work therefore provides a practical electrolyte-design principle for reconciling rapid Li^+ transport with stable graphite operation in high-rate lithium-ion batteries.

Electronic Supplementary Material:
Supplementary material (Figures S1–S17) is available in the online version of this article at https://doi.org/10.26599/NR.2026.94909304.

Data availability

All data needed to support the conclusions in the paper are presented in the manuscript and Electronic Supplementary Material. Additional data related to this paper may be requested from the corresponding authors upon reasonable request.

Acknowledgements

This work was supported by the National Natural Science Foundation of China (42406221 to Q.Y, 22679087 to M.B.Z, 5247221 to Z.H.L), the Guangdong Provincial Pearl River Talents Program (Grant nos. 2023QN10C221 to Y.P), the Natural Science Foundation of Jiangsu Province (BK20220912 to Z.H.L). The authors would also like to acknowledge the High-Performance Computing Platform of Nanjing University of Aeronautics and Astronautics, Center for Microscopy and Analysis at Nanjing University of Aeronautics and Astronautics.

Declaration of competing interest

All the contributing authors report no conflict of interests in this work.

Author contribution statement

Tian Gao: Investigation, Data curation, Formal analysis, Writing-original draft. Qiang Yu: Conceptualization, Methodology, Supervision, Writing – review & editing, Funding acquisition. Zicheng Zhao: Investigation, Data curation. Xiaowang Tu: Methodology, Data curation. Zhenming Xu: Formal analysis, Investigation. Mingbo Zheng: Data curation, Methodology. Jianyu Shi: Data curation, Formal analysis. Yujie Zhou: Data curation, Investigation. Yi Pei: Methodology, Formal analysis. Zhenhui Liu: Writing – review & editing, Supervision, Funding acquisition. Junfeng Chen: Writing – review & editing, Methodology, Supervision.

Use of AI statement

"None."

References

[1] Lei, S.; Zeng, Z.; Cheng, S.; Xie, J. Fast-charging of lithium-ion batteries: A review of electrolyte design aspects. *Battery Energy* **2023**, *2*, 20230018.

[2] He, J.; Meng, J.; Huang, Y. Challenges and recent progress in fast-charging lithium-ion battery materials. *J. Power Sources* **2023**, *570*, 232965.

[3] Hu, W.; Pan, Y.; Zhong, M.; Wang, L.; Jiang, W.; He, X. Multiscale design strategies for fast-charging graphite anodes in lithium-ion batteries. *Small* **2026**, *22*, e73273.

[4] Song, C.; Han, S. H.; Moon, H.; Choi, N.-S. Unlocking fast-charging capabilities of lithium-ion batteries through liquid electrolyte engineering. *EcoMat* **2024**, *6*, e12476.

[5] Fan, Z.; Zhang, J.; Wu, L.; Yu, H.; Li, J.; Li, K.; Zhao, Q. Solvation structure dependent ion transport and desolvation mechanism for fast-charging Li-ion batteries. *Chem. Sci.* **2024**, *15*, 17161–17172.

[6] Li, J.; Guo, C.; Tao, L.; Meng, J.; Xu, X.; Liu, F.; Wang, X. Electrode and electrolyte design strategies toward fast-charging lithium-ion batteries. *Adv. Funct. Mater.* **2024**, *34*, 2409097.

[7] Chen, S.; Wang, J.; Zhang, M.; et al. Recent advances in lithium-ion battery electrolytes: Theory, materials, and applications. *Energy Storage Mater.* **2021**, *36*, 186–212.

[8] Wu, H.; Jia, H.; Wang, C.; Zhang, J. G.; Xu, W. Recent progress in understanding solid electrolyte interphase on lithium metal anodes. *Adv. Energy Mater.* **2021**, *11*, 2003092.

[9] Wang, Q.; Jiang, L.; Yu, Y.; Sun, J. Progress in understanding SEI formation and regulation for lithium-ion batteries. *Energy Storage Mater.* **2021**, *35*, 332–349.

[10] Cao, X.; Jia, H.; Xu, W.; Zhang, J. G. Review of electrolyte design strategies for stable interphases in lithium batteries. *Adv. Energy Mater.* **2021**, *11*, 2003865.

[11] An, S. J.; Li, J.; Daniel, C.; Mohanty, D.; Nagpure, S.; Wood, D. L. The state of understanding of the lithium-ion-battery graphite solid electrolyte interphase (SEI) and its relationship to formation cycling. *Carbon* **2016**, *105*, 52–76.

[12] Heiskanen, S. K.; Kim, J.; Lucht, B. L. Generation and evolution of the solid electrolyte interphase of lithium-ion batteries. *Joule* **2019**, *3*, 2322–2333.

Just Accepted

[13] Ren, X.; Chen, S.; Lee, H.; Mei, D.; Engelhard, M. H.; Burton, S. D.; Zhao, Y.; Zheng, J.; Li, Q.; Ding, M. S.; Schroeder, M.; Xu, K.; Zhang, J. G.; Xu, W. Localized high-concentration electrolytes for high-voltage lithium-ion batteries. *Chem* **2020**, *6*, 2973–3000.

[14] Borodin, O.; Self, J.; Persson, K. A.; Ceder, G.; Wang, C. Uncharted waters of lithium solvation: From liquids to solids. *Joule* **2020**, *4*, 69–100.

[15] Yamada, Y.; Wang, J.; Ko, S.; Watanabe, E.; Yamada, A. Advances and issues in developing salt-concentrated battery electrolytes. *Nat. Energy* **2020**, *5*, 1–14.

[16] Xiao, H.; Zhao, J.; Gao, Q.; et al. Recent advances in fast-charging lithium-ion batteries: Mechanism, materials, and future opportunities. *Chem. Eng. J.* **2025**, *506*, 159927.

[17] Shu, W.; Zeng, Z.; Qin, M.; et al. Perspective on fast-charging lithium-ion batteries: Mechanism, detection, and suppression of graphite anode lithium plating. *Energy Storage Mater.* **2025**, *81*, 104479.

[18] Zhang, X. Q.; Cheng, X. B.; Zhang, Q. Advances in electrolyte design for fast-charging lithium-ion batteries. *Energy Environ. Sci.* **2021**, *14*, 1506–1530.

[19] Wang, S.; Shi, J.; Liu, Z.; Xia, Y. Advanced ether-based electrolytes for lithium-ion batteries. *Adv. Energy Mater.* **2024**, *14*, 2401526.

[20] Zhang, S. S. Adoption of dimethoxyethane and 1,3-dioxolane in electrolyte for fast charging of Li-ion battery. *Batteries* **2023**, *9*, 466.

[21] Xiang, J.; Lu, Y.-C. Ether-based high-voltage lithium metal batteries: the road to commercialization. *ACS Nano* **2024**, *18*, 10726–10737.

[22] Holoubek, J.; Liu, H.; Wu, Z.; Yin, Y.; Xing, X.; Cai, G.; Chen, S.; Yu, H.; Li, H.; Liu, P.; et al. Tailoring electrolyte solvation chemistry for lithium batteries. *Chem. Soc. Rev.* **2022**, *51*, 8739–8770.

[23] Zhang, X. Q.; Chen, X.; Hou, L. P.; Li, B. Q.; Cheng, X. B.; Zhang, Q. Regulating the solvation structure of ether electrolytes for stable lithium metal batteries. *Adv. Energy Mater.* **2021**, *11*, 2003301.

[24] Wang, F.; Borodin, O.; Gao, T.; Fan, X.; Sun, W.; Han, F.; Faraone, A.; Dura, J. A.; Xu, K.; Wang, C. Highly reversible zinc metal anode enabled by a water-in-salt electrolyte. *Nat. Mater.* **2022**, *21*, 1230–1237.

[25] Zhang, J.; Zhang, Y.; et al. Self-terminating, heterogeneous solid-electrolyte interphase enables reversible Li-ether cointercalation in graphite anodes. *Proc. Natl. Acad. Sci. U.S.A.* **2024**, *121*, e2313096121.

[26] Kondo, Y.; Nakajima, H.; Katayama, Y.; et al. Electrolyte Li^+ chemical potential correlates with graphite negative electrode reactions in lithium-ion batteries. *Adv. Mater.* **2025**, e14060.

[27] Kim, H.; Hong, J.; Park, K. Y.; et al. Solvated ion intercalation in graphite: Sodium and beyond. *ACS Energy Lett.* **2020**, *5*, 1584–1590.

[28] Xu, K.; Von Cresce, A.; Lee, U. Differentiating contributions to "ion transfer" barrier from interphasial resistance and Li^+ desolvation at electrolyte/graphite interface. *Langmuir* **2010**, *26*, 11538–11543.

[29] Chen, K.; Shen, X.; Luo, L.; Chen, H.; Cao, R.; Feng, X.; Chen, W.; Fang, Y. Correlating the solvating power of solvents with the strength of ion-dipole interaction in electrolytes of lithium-ion batteries. *Angew. Chem.* **2023**, *135*, e202312373.

[30] Xiao, H.; Li, X.; Fu, Y. Advances in anion chemistry in the electrolyte design for better lithium batteries. *Nano-Micro Lett.* **2025**, *17*, 149.

[31] Ren, X.; Gao, P.; Zou, L.; Jiao, S.; Cao, X.; Zhang, X.; Jia, H.; Engelhard, M. H.; et al. Role of inner solvation sheath within salt-solvent complexes in tailoring electrode/electrolyte interphases for lithium metal batteries. *Proc. Natl. Acad. Sci. U.S.A.* **2020**, *117*, 28603–28613.

[32] Karbak, M.; Yim, K.; Meng, Y. S.; Shao, Y.; Xu, W. Weakly solvating electrolytes: a solvation-centric paradigm for rechargeable metal batteries. *Chem. Sci.* **2025**, *16*, 20694–20717.

[33] Gao, W.; Peng, Y.; Lu, Y.; Liu, X.; Xu, Y.; Yang, K.; Wu, Y.; He, J. Localized high-concentration electrolytes for rechargeable batteries. *Energy Storage Mater.* **2025**, *80*, 104378.

[34] Peng, L.; Wu, X.; Jia, M.; Qian, W.; Zhang, X.; Zhou, N.; Zhang, L.; Jian, C. Solvating power regulation enabled low concentration electrolyte for lithium batteries. *Sci. Bull.* **2022**, *67*, 2235–2244.

[35] Zheng, H.; Xiang, H.; Jiang, F.; Liu, Y.; Sun, Y.; Liang, X.; Feng, Y.; Yu, Y. Lithium difluorophosphate-based dual-salt low concentration electrolytes for lithium metal batteries. *Adv. Energy Mater.* **2020**, *10*, 2001440.

[36] Lu, T.; Chen, F. Multiwfn: A multifunctional wavefunction analyzer. *J. Comput. Chem.* **2012**, *33*, 580–592.

[37] Lu, T. A comprehensive electron wavefunction analysis toolbox for chemists: Multiwfn. *J. Chem. Phys.* **2024**, *161*, 082503.

[38] Wu, Y.; Hu, Q.; Liang, H.; Wang, A.; Xu, H.; Wang, L.; He, X. Electrostatic potential as solvent descriptor to enable rational electrolyte design for lithium batteries. *Adv. Energy Mater.* **2023**, *13*, 2300259.

[39] Weppner, W.; Huggins, R. A. Determination of the kinetic parameters of mixed-conducting electrodes and application to the system Li3Sb. *J. Electrochem. Soc.* **1977**, *124*, 1569–1578.

[40] Chen, Z.; Chen, T.; Zhang, X.; Chen, G.; Moyo, O.; Sun, M.; Sun, H.; Zhu, Y.; Zhang, X. Advances in electrochemical synthesis of urea from CO_2 and nitrogen-containing precursors. *Chem. Commun.* **2026**, *62*, 12281–12307.

[41] Du, Y.; Zhong, Z.; Shi, Z.; Zhou, L.; Pan, S.; Xu, X.; Liu, Y.; Xiong, D.; Wang, K. Dual-ligand engineered CoNi alloy/N-doped carbon nanotubes bifunctional ORR/OER electrocatalyst for long-lifespan rechargeable Zn-air batteries. *J. Colloid Interface Sci.* **2025**, *683*, 631–640.

[42] Gauthier, N.; Courrèges, C.; Demeaux, J.; Tessier, C.; Martinez, H. Probing the in-depth distribution of organic/inorganic molecular species within the SEI of LTO/NMC and LTO/LMO batteries: a complementary ToF-SIMS and XPS study. *Appl. Surf. Sci.* **2020**, *501*, 144266.

[43] McShane, E. J.; Bergstrom, H. K.; Weddle, P. J.; Brown, D. E.; Colclasure, A. M.; McCloskey, B. D. Quantifying graphite solid-electrolyte interphase chemistry and its impact on fast charging. *ACS Energy Lett.* **2022**, *7*, 2734–2744.

Just Accepted

Electronic Supplementary Material

Salt-regulated interfacial desolvation suppresses Co-intercalation of strongly coordinating ether-based electrolytes for fast-charging lithium-ion batteries

Tian Gao [1], Xiaowang Tu [1], Zicheng Zhao [1], Qiang Yu [2] ✉, Zhenming Xu [1], Mingbo Zheng [1], Jianyu Shi [1], Yujie Zhou [1], Junfeng Chen [3] ✉, Yi Pei [4], Zhenhui Liu [1] ✉

[1] College of Material Science and Engineering, Jiangsu Key Laboratory of Materials and Technology for Energy Conversion, Nanjing University of Aeronautics and Astronautics, Nanjing 210016, China
[2] Laoshan Laboratory, Qingdao 266237, China
[3] School of Materials Science and Engineering, Fuzhou University, Fuzhou 350108, China, State Key Laboratory of Green and Efficient Development of Phosphorus Resources, Fuzhou University, Fuzhou 350108, China
[4] Shenzhen Research Institute, Nanjing University of Aeronautics and Astronautics, Shenzhen 518110, China

Supporting information to https://doi.org/10.26599/NR.2026.94909304

Just Accepted

Address correspondence to Qiang Yu, qyu1@lsnl.cn; Zhenhui Liu, lzh0328@nuaa.edu.cn; Junfeng Chen, chenjunfeng@fzu.edu.cn

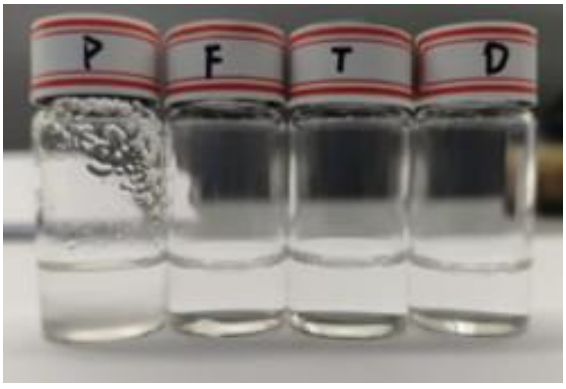


Figure S1. $LiPF_6$, LiFSI, LiTFSI, and LiDFOB electrolytes in DME/FEC (95/5, v/v).

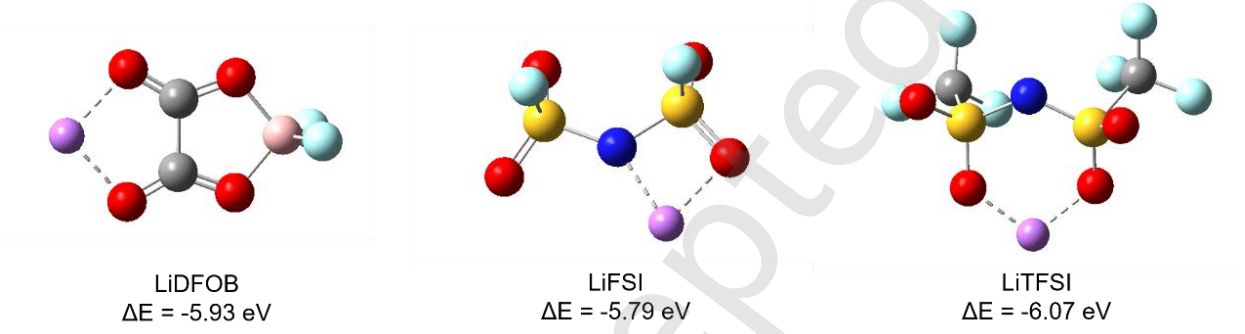


Figure S2. Calculated binding energies between Li^+ and different anions ($DFOB^-$, $TFSI^-$, and FSI^-).

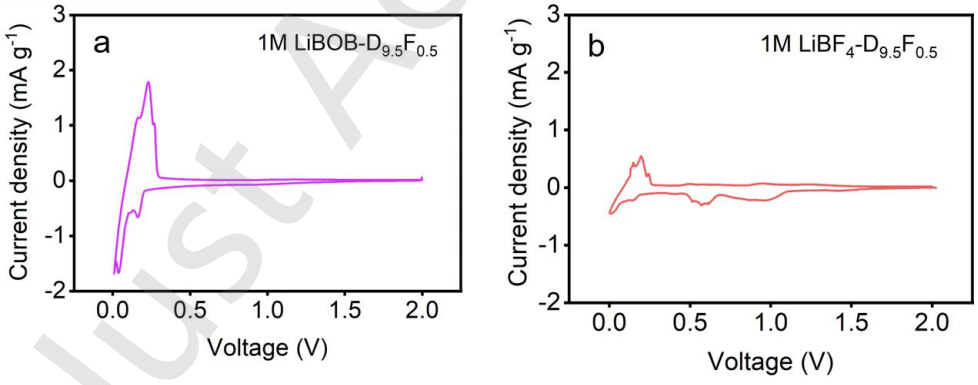


Figure S3. Cyclic voltammograms of graphite in (a) 1 M LiBOB-$D_{9.5}F_{0.5}$ and (b) 1 M LiBF4-$D_{9.5}F_{0.5}$ at 0.2 mV s^{-1}.

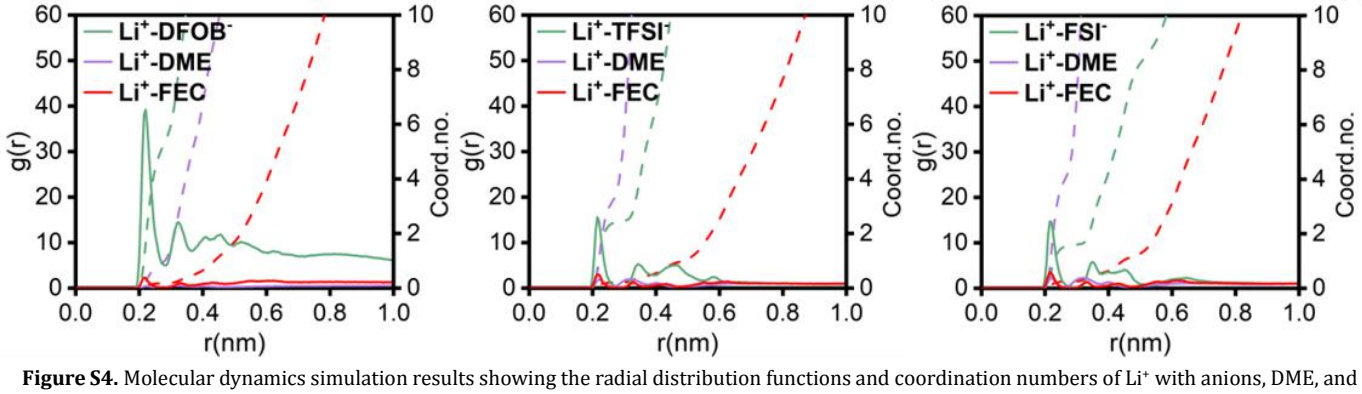


Figure S4. Molecular dynamics simulation results showing the radial distribution functions and coordination numbers of Li^+ with anions, DME, and FEC in different DME-based electrolytes.

Just Accepted

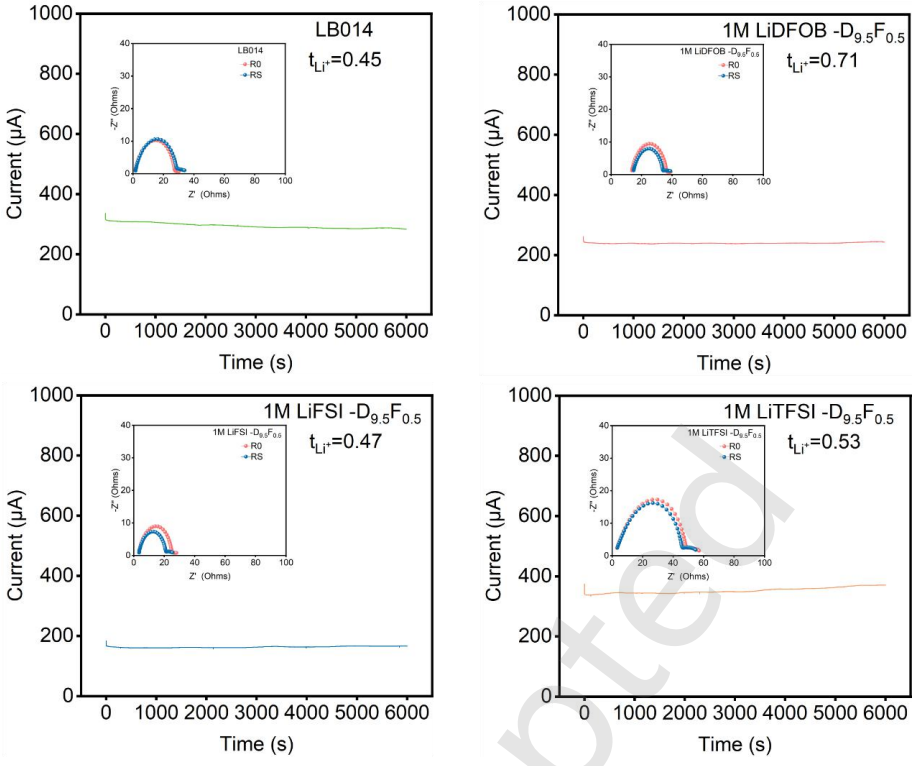


Figure S5. Potentiostatic polarization curves and corresponding EIS spectra before and after polarization for determining the Li^+ transference numbers of LB014 and 1 M LiDFOB, LiFSI, and LiTFSI electrolytes in DME/FEC (95/5, v/v).

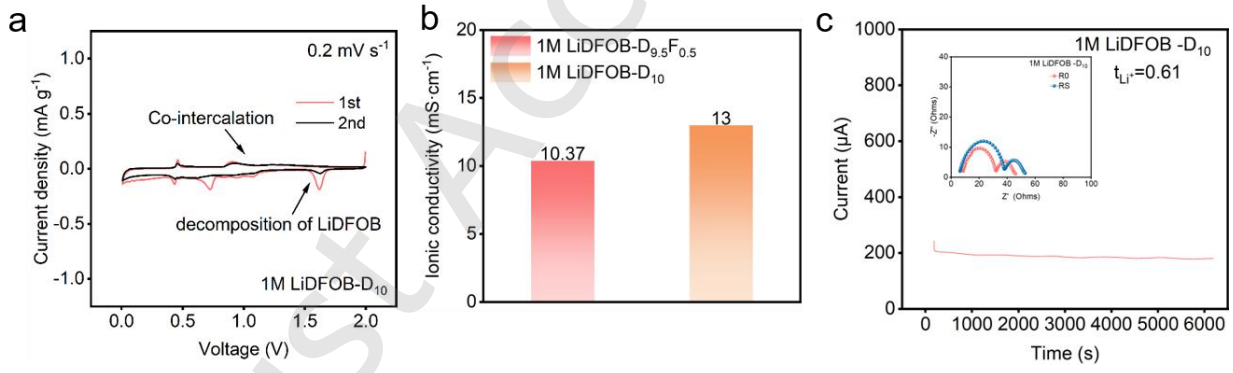


Figure S6. Characterization of the FEC-free 1 M LiDFOB-D10 electrolyte. (a) Cyclic voltammograms of graphite in 1 M LiDFOB-D10 at 0.2 mV s^{-1}. (b) Ionic conductivity of 1 M LiDFOB-$D_{9.5}F_{0.5}$ and 1 M LiDFOB-D10 at 25 °C. (c) Potentiostatic polarization of a Li||Li symmetric cell in 1 M LiDFOB-D10 at an applied voltage of 10 mV, with the EIS spectra recorded before and after polarization shown in the inset; the derived Li^+ transference number is 0.61.

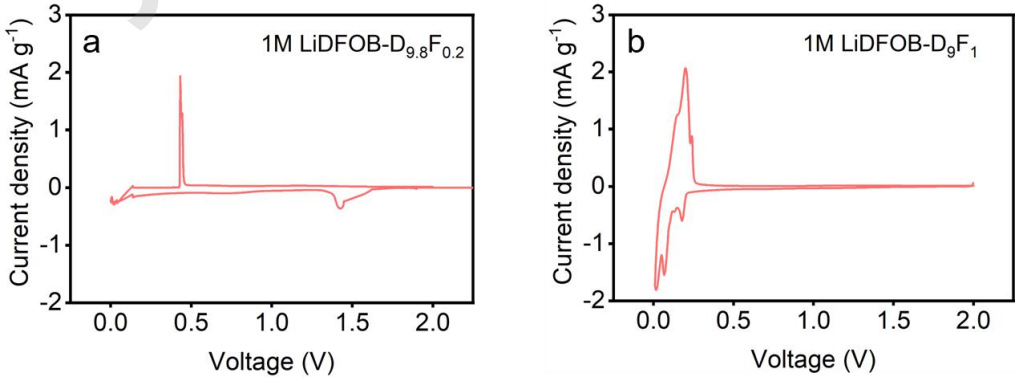


Figure S7. Cyclic voltammograms of graphite in (a) 1 M LiDFOB-$D_{9.8}F_{0.2}$ (2 vol% FEC) and (b) 1 M LiDFOB-D_9F_1 (10 vol% FEC) at 0.2 mV s^{-1}.

Just Accepted

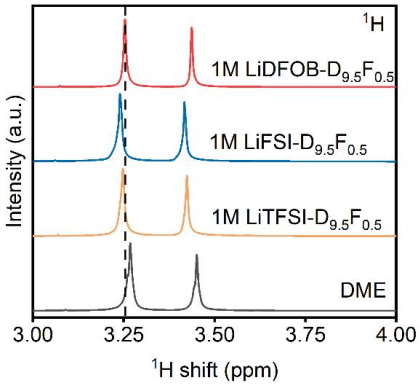


Figure S8. ^{1}H NMR spectra of pristine DME and 1 M LiDFOB, LiTFSI, and LiFSI electrolytes.

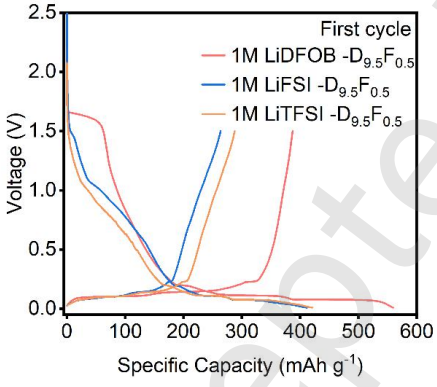


Figure S9. First-cycle galvanostatic charge–discharge voltage profiles of Gr||Li half-cells using 1 M LiDFOB, LiFSI, and LiTFSI electrolytes in DME/FEC (95/5, v/v).

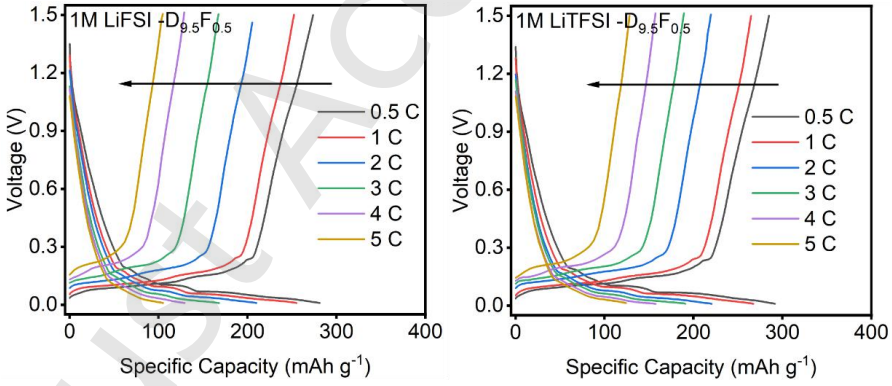


Figure S10. Rate-dependent galvanostatic charge–discharge voltage profiles of Gr||Li half-cells using 1 M LiFSI and 1 M LiTFSI electrolytes in DME/FEC (95/5, v/v).

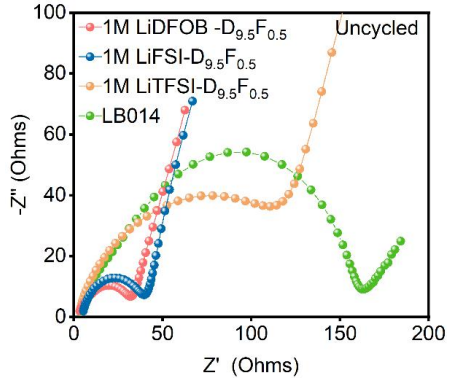


Figure S11. Nyquist plots of uncycled Gr||Li cells using 1 M LiDFOB, LiFSI, and LiTFSI electrolytes in DME/FEC (95/5, v/v), together with the conventional carbonate electrolyte LB014.

Just Accepted

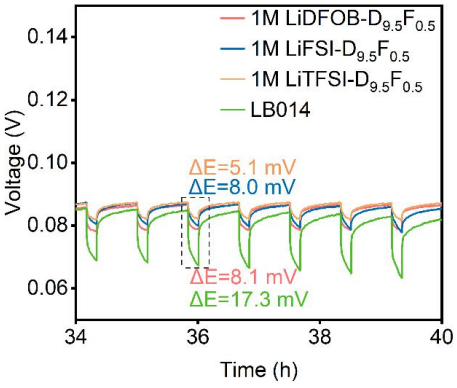


Figure S12. Enlarged GITT pulse–relaxation voltage profiles of Gr||Li cells using 1 M LiDFOB, LiFSI, and LiTFSI electrolytes in DME/FEC (95/5, v/v) and the conventional carbonate electrolyte LB014.

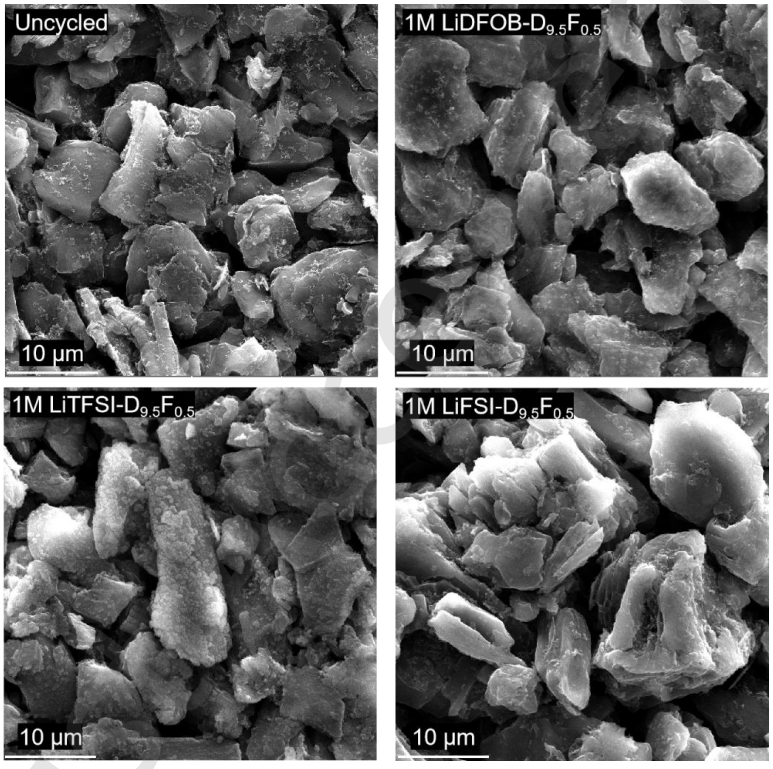


Figure S13. Microscale SEM images showing the morphological evolution of graphite particles after the first cycle in LiDFOB, LiTFSI, and LiFSI-based DME/FEC electrolytes.

Journal Pre-proof

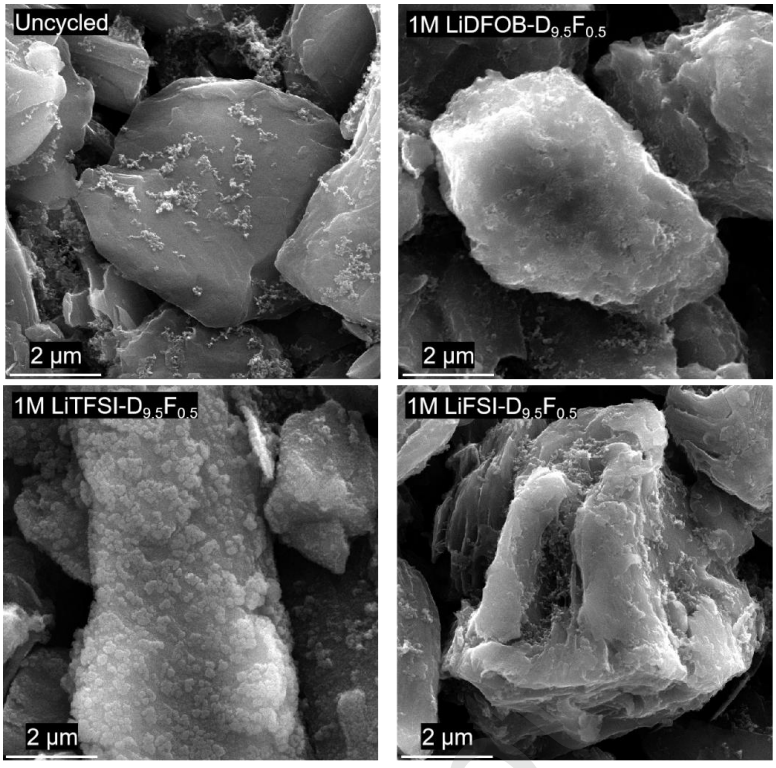


Figure S14. High-magnification SEM images showing the surface morphology evolution of graphite electrodes after the first cycle in LiDFOB, LiTFSI, and LiFSI-based DME/FEC electrolytes.

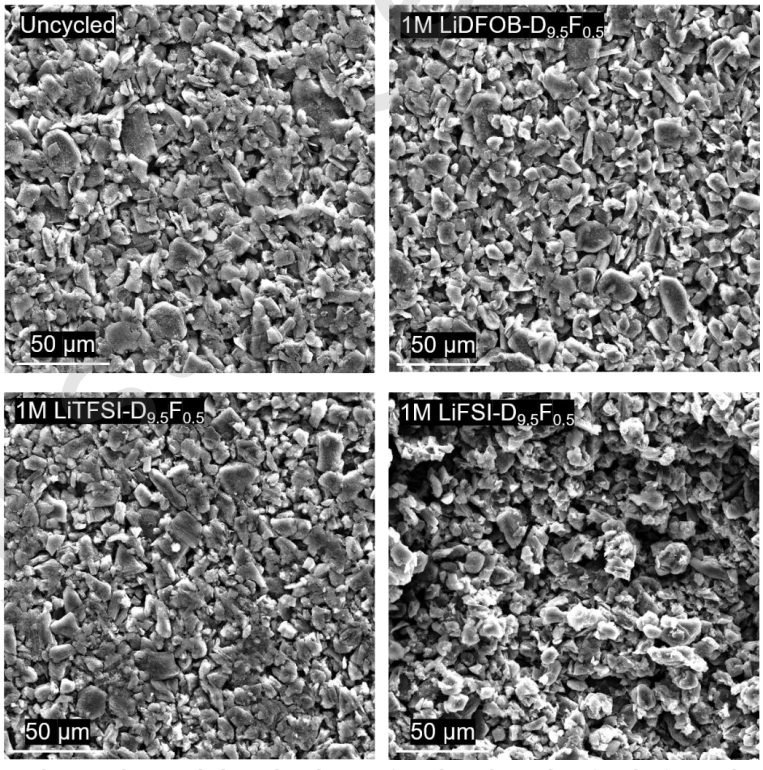


Figure S15. Large-area SEM images showing the morphological evolution of graphite electrodes after the first cycle in LiDFOB, LiTFSI, and LiFSI-based DME/FEC electrolytes.

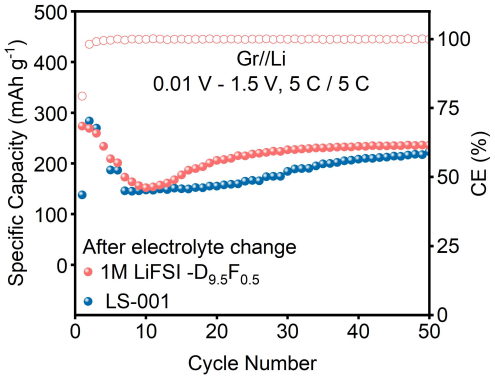


Figure S16. Cycling performance of Gr||Li cells at 5 C after the electrolyte was replaced from 1 M LiDFOB-$D_{9.5}F_{0.5}$ to 1 M LiFSI-$D_{9.5}F_{0.5}$ or LS-001 (1 M LiTFSI in 1,3-dioxolane/DME, 1:1, v/v).

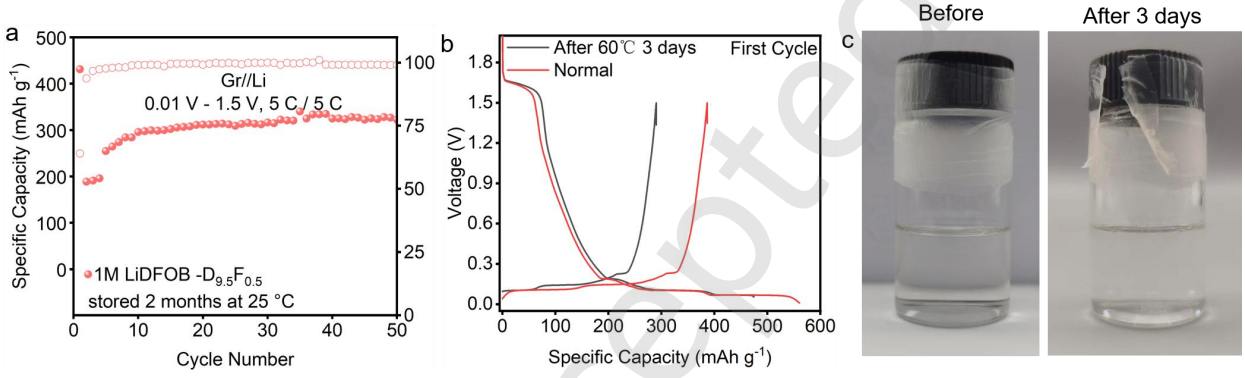


Figure S17. (a) Cycling performance of Gr||Li cells at 5 C using 1 M LiDFOB-D9.5F0.5 stored at 25 °C for two months. (b) First-cycle charge–discharge voltage profiles of Gr||Li cells using 1 M LiDFOB-D9.5F0.5 before and after storage at 60 °C for three days. (c) Optical photographs of the electrolyte before (left) and after (right) storage at 60 °C for three days; the liquid remains clear and colorless, with no visible precipitate or phase separation.

Just Accepted